High-Resolution Angle Tracking for Mobile Wideband Millimeter-Wave Systems with Antenna Array Calibration

Dalin Zhu, Junil Choi, Qian Cheng, Weimin Xiao, and Robert W. Heath Jr.

***Abstract*—Millimeter-wave (mmWave) systems use directional beams to support high-rate data communications. Small misalignment between the transmit and receive beams (e.g., due to the mobility) can result in significant drop of the received signal quality especially in line-of-sight communication channels. In this paper, we propose and evaluate high-resolution angle tracking strategies for wideband mmWave systems with mobility. We custom design pairs of auxiliary beams as the tracking beams, and use them to capture the angle variations, towards which the steering directions of the data beams are adjusted. Different from conventional beam tracking designs, the proposed framework neither depends on the angle variation model nor requires an on-grid assumption. For practical implementation of the proposed methods, we examine the impact of the array calibration errors on the auxiliary beam pair design. Numerical results reveal that by employing the proposed methods, good angle tracking performance can be achieved under various antenna array configurations, channel models, and mobility conditions.**

I. Introduction

The small array form factor at millimeter-wave (mmWave) frequencies enables the use of large antenna arrays to generate highly directional beams. This allows array gain for improved received signal power and also reduces mean interference levels [1]-[5]. For the most benefits from beamforming, accurate channel direction information such as the channel's angle-of-departures (AoDs) and angle-of-arrivals (AoAs) is required at both the base station (BS) and user equipment (UE) sides. Further, due to the UE's mobility, slight misalignments of the transmit and receive beams with the channel's AoDs and AoAs may result in significant performance loss at mmWave frequencies in line-of-sight (LOS) communication channels. Hence, accurate beam or angle tracking designs are required to better capture the channel variations and enable reliable mmWave communications in fast-varying environments.

Grid-of-beams based beam training is the defacto approach for configuring transmit and receive beams; variations are used in IEEE 802.11ad systems [6], [7] and will be used in 5G [8]. Beam tracking approaches that support grid-of-beams have been developed in [6], [7], [9], [10], but the performance depends on the grid resolution, leading to high complexity, tracking overhead, and access delay. In [11], [12], a priori-aided angle tracking strategies were proposed. By combining the temporal variation law of the AoD and AoA of the LOS path with the sparse structure of the mmWave channels, the channels obtained during the previous time-slots are used to predict the support (the index set of non-zero elements in a sparse vector) of the channel. The time-varying parameters corresponding to the support of the channel are then tracked for the subsequent time-slots. To track the non-LOS (NLOS) paths, the classical Kalman filter can be employed by first eliminating the influence of the LOS path [13]. In [14], the idea of Kalman filter was exploited as well when designing the angle tracking and abrupt change detection algorithms. In [15], the extended Kalman filter was used to track the channel's AoDs and AoAs by only using the measurement of a single beam pair. The angle tracking algorithms developed in [11]-[15], however, depend on specific modeling of the geometric relationship between the BS and UE and the angle variations.

In this paper, we develop high-resolution angle tracking algorithms through the auxiliary beam pair design for mobile wideband mmWave systems under the analog architecture. In the employed analog architecture, the BS uses a small number of radio frequency (RF) chains to drive a large number of antenna elements, and forms the tracking beams in the analog domain. We propose and analyze new angle tracking procedures, where the basic principles follow those in [16], [17] with moderate modifications based on the employed array configurations and pilot signal structures. In our previous work [16], [17], we exploited the idea of auxiliary beam pair design to estimate both the narrowband and wideband mmWave channels with and without dual-polarization. The proposed approaches, however, were only applied to the angle estimation, and not specifically designed for the angle tracking. We summarize the main contributions of the paper as follows:

- We provide detailed design procedures of the auxiliary beam pair-assisted angle tracking approaches in wideband mmWave systems. We propose several angle tracking design options and differentiate them in terms of triggering device, feedback information, and information required at the UE side.
- We reveal several important implementation aspects of

Dalin Zhu and Robert W. Heath Jr. are with the Department of Electrical and Computer Engineering, The University of Texas at Austin, Austin, TX, 78712 USA, e-mail: {dalin.zhu, rheath}@utexas.edu.

Junil Choi is with the Department of Electrical Engineering, Pohang University of Science and Technology (POSTECH), Pohang, Gyeongbuk 37673 Korea, e-mail: junil@postech.ac.kr.

Qian Cheng and Weimin Xiao are with the Wireless Research and Standards Department, Huawei R&D USA, Rolling Meadows, IL, 60008 USA, e-mail: {q.cheng, weimin.xiao}@huawei.com

This work was supported in part by a gift from Huawei Technologies, in part by the National Science Foundation under Grant No. ECCS-1711702, CNS-1702800 and CNS-1731658, and in part by the National Research Foundation (NRF) grant funded by the MSIT of the Korea government (2018R1A4A1025679).

TABLE I
SUMMARY OF NOTATIONS AND DESCRIPTIONS

MIMO channel matrix	$\boldsymbol{H}$
Transmit and receive array response vectors	$\boldsymbol{a}_{\mathrm{t}}(\cdot,\cdot)$ and $\boldsymbol{a}_{\mathrm{r}}(\cdot)$
Elevation and azimuth AoDs for path-r	μ_r and ϕ_r
AoA for path-r	φ_r
Elevation and azimuth transmit spatial frequencies for path-r	θ_r and ψ_r
Receive spatial frequency for path-r	ν_r
Transmit signal vector (pilot signals for tracking)	$\boldsymbol{s}$
Received signal vector	$\boldsymbol{y}$
Correlation between $\boldsymbol{y}$ and reference ZC sequence	Λ
Boresights of azimuth and elevation auxiliary beam pairs	η_{az} and η_{el}
Power ratio metric	ζ
Received signal strength	χ
Root indices for ZC sequences design	i_0, i_1
ZC sequence length	N_{ZC}
Time-slot index and total number of time-slots	t and T
Phase and amplitude errors matrices	$\boldsymbol{P}$ and $\boldsymbol{A}$

deploying our proposed angle tracking algorithms in practical systems, including impacts of multi-user interference, multi-path interference and noise impairment on the tracking performances, and tracking sequences design for the auxiliary beam pair structure. We use conceptual and numerical examples to explain our proposed potential solutions in addressing these issues. We also calculate the computational complexity and signaling overhead for the proposed designs.

- We characterize the impact of the radiation pattern impairments caused by the hardware flaw before and after the array calibration on our proposed methods. This hardware flaw is mainly brought by the antenna element tolerances and manufacturing inaccuracies, causing non-uniform amplitude and phase characteristics of the beam patterns. We first exhibit that relatively large phase and amplitude errors would contaminate the angle tracking performances of the proposed algorithms, resulting in increased tracking error probability and reduced spectral efficiency. We custom design a receive combining based array calibration method for the analog architecture. Note that since the radiation pattern impairments resulted from manufacturing inaccuracies/imperfections are long-term characteristics [18, Chapter 2], we focus on off-line array calibration in this paper.

We organize the rest of this paper as follows. In Section II, we first describe the employed system and wideband channel models; we then illustrate the frame structure and conventional grid-of-beams based beam tracking design for mmWave systems. In Section III, we explain detailed design principles and procedures of the proposed high-resolution angle tracking strategies; we also address several important implementation issues of deploying the proposed algorithms in practice, such as computational complexity, signaling overhead, tracking sequence design and multi-user interference. In Section IV, we discuss the developed array calibration method and its impact on the proposed angle tracking designs. In Section V, we present numerical results to validate the effectiveness of the proposed techniques. Finally, we draw our conclusions in Section VI.

Notations: $\boldsymbol{A}$ is a matrix; $\boldsymbol{a}$ is a vector; a is a scalar; $|a|$ is the magnitude of the complex number a; $(\cdot)^{\mathrm{T}}$ and $(\cdot)^*$ denote transpose and conjugate transpose; $\boldsymbol{I}_N$ is the $N \times N$ identity matrix; $\boldsymbol{1}_{M\times N}$ represents the $M \times N$ matrix whose entries are all ones; $\mathcal{N}_{\mathrm{c}}(\boldsymbol{a}, \boldsymbol{A})$ is a complex Gaussian vector with mean $\boldsymbol{a}$ and covariance $\boldsymbol{A}$; $\mathbb{E}[\cdot]$ is used to denote expectation; $\otimes$ is the Kronecker product; and $\mathrm{diag}(\cdot)$ is the diagonalization operation. We provide common definitions used throughout the paper in Table I.

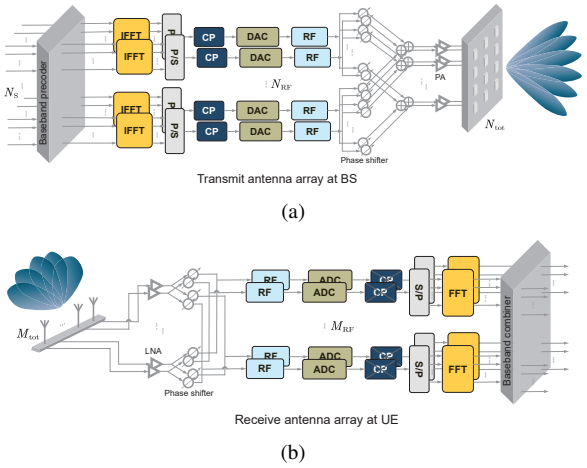

(a)

(b)

Fig. 1. (a) Shared-array architecture employed at the BS with N_{RF} RF chains and a total of N_{tot} transmit antenna elements configured in a uniform planar array. (b) Shared-array architecture employed at the UE with M_{RF} RF chains and a total of M_{tot} receive antenna elements configured in a uniform linear array.

II. System Model and Conventional Beam Tracking Design

In this section, we first present the employed system model including the transceiver architecture, antenna array configurations, and wideband mmWave channel model. We then illustrate the conventional grid-of-beams based beam tracking design along with an introduction to the frame structure.

A. Transceiver architecture, antenna array configurations, and received signal model

We consider a precoded MIMO-OFDM system with N subcarriers and a hybrid precoding transceiver structure as shown in Figs. 1(a) and 1(b). A BS equipped with $N_{\rm tot}$ transmit antennas and $N_{\rm RF}$ RF chains transmits $N_{\rm S}$ data streams to a UE equipped with $M_{\rm tot}$ receive antennas and $M_{\rm RF}$ RF chains. As can be seen from Fig. 1, in a shared-array architecture, all antenna elements are jointly controlled by all RF chains sharing the same network of phase shifters. Further, we assume that a uniform planar array (UPA) is adopted at the BS, and a uniform linear array (ULA) is employed at the UE. The proposed methods are custom designed for uniform arrays, but can be extended to other array geometries by reconfiguring the beamforming vectors. The proposed methods are suited for both co-polarized and cross-polarized arrays [17], though we focus on co-polarized array setup in this paper.

Based on the employed transceiver architecture, we now develop the baseband received signal model for our system after beamforming and combining. Let $\boldsymbol{s}[k]$ denote an $N_{\rm S}\times 1$ baseband transmit symbol vector such that $\mathbb{E}\left[\boldsymbol{s}[k]\boldsymbol{s}^*[k]\right] = \boldsymbol{I}_{N_{\rm S}}$ and $k=0,\cdots,N-1$. The data symbol vector $\boldsymbol{s}[k]$ is first precoded using an $N_{\rm RF}\times N_{\rm S}$ digital baseband precoding matrix $\boldsymbol{F}_{\rm BB}[k]$ on the k-th subcarrier, resulting in $\boldsymbol{d}[k] = [d_1[k],\cdots,d_{N_{\rm RF}}[k]]^{\rm T} = \boldsymbol{F}_{\rm BB}[k]\boldsymbol{s}[k]$. In this paper, we set $N_{\rm RF}=N_{\rm S}$ and $\boldsymbol{F}_{\rm BB}[k]=\boldsymbol{I}_{N_{\rm S}}$ because the channel tracking is conducted in the analog domain. Note that similar analog-only assumption applies to the UE side as well. For data communications, the digital baseband processing can be further optimized to enhance the system capacity. For instance, leveraging the angle estimation/tracking results, we can first construct the analog beamforming and combining vectors as matched filters to the array response vectors. Building on top of the analog beamformers and combiners, we can then optimize the baseband precoding and combining matrices according to a certain metric, e.g., the effective received signal power metric in [19]. The transmit symbols are then transformed to the time-domain via $N_{\rm RF}$, N-point IFFTs, generating the discrete-time signal sample $x_{n_{\rm R}}[n] = \sum_{k=0}^{N-1} d_{n_{\rm R}}[k]e^{{\rm j}\frac{2\pi k}{N}n}$, where $n_{\rm R}=1,\cdots,N_{\rm RF}$. Before applying an $N_{\rm tot}\times N_{\rm RF}$ wideband analog precoding matrix $\boldsymbol{F}_{\rm RF}$, a cyclic prefix (CP) with length D is added to the data symbol blocks such that D is greater than or equal to the maximum delay spread of the multi-path channel. Denote by $\boldsymbol{x}[n_{\rm c}] = [x_1[n_{\rm c}],\cdots,x_{N_{\rm RF}}[n_{\rm c}]]^{\rm T}$, where $n_{\rm c}=N-D,\cdots,N-1,0,\cdots,N-1$ due to the insertion of the CP. We can then express the discrete-time transmit signal model as $\boldsymbol{x}_{\rm cp}[n_{\rm c}] = \boldsymbol{F}_{\rm RF}\boldsymbol{x}[n_{\rm c}]$. To maintain the total transmit power constraint, $\left[[\boldsymbol{F}_{\rm RF}]_{:,n_{\rm R}}[\boldsymbol{F}_{\rm RF}]^*_{:,n_{\rm R}}\right]_{i,i} = \frac{1}{N_{\rm tot}}$ is satisfied with $i=1,\cdots,N_{\rm tot}$.

At the UE side, after combining with an $M_{\rm tot}\times M_{\rm RF}$ analog combining matrix $\boldsymbol{W}_{\rm RF}$, the CP is removed. The received data symbols are then transformed from the time-domain to the frequency-domain via $M_{\rm RF}$, N-point FFTs. Denote the frequency-domain $M_{\rm tot}\times N_{\rm tot}$ channel matrix by $\boldsymbol{H}[k]$. We can then express the discrete-time received signal as

$$\boldsymbol{y}[k] = \boldsymbol{W}^*_{\rm RF}\boldsymbol{H}[k]\boldsymbol{F}_{\rm RF}\boldsymbol{d}[k] + \boldsymbol{W}^*_{\rm RF}\boldsymbol{n}[k]. \tag{1}$$

The noise vector $\boldsymbol{n}\sim\mathcal{N}_c(\boldsymbol{0}_{M_{\rm tot}},\sigma^2\boldsymbol{I}_{M_{\rm tot}})$ and $\sigma^2=1/\gamma$, where γ represents the target signal-to-noise ratio (SNR) before the transmit beamforming. Note that the number of simultaneous data streams would be around two in practice while the numbers of RF chains used by the BS and UE may be much larger than that. Since the number of RF chains used by the BS/UE for the proposed angle tracking is two, the number of RF chains is not a limitation for the proposed angle tracking technique.

B. Wideband channel model

We employ a spatial geometric model to characterize the wideband mmWave channel. The spatial geometric channel models have been adopted in Long-Term Evolution (LTE) systems for various deployment scenarios [20]. In Section V, we use practical channel parameters obtained via measurements to evaluate the proposed methods, though we employ the spatial geometric channel model to analytically explain the core idea. We assume that the channel has $N_{\rm r}$ paths, and each path r has azimuth and elevation AoDs ϕ_r, μ_r, and AoA φ_r in this paper. Let $p(\tau)$ denote the combined effect of filtering and pulse-shaping for $T_{\rm s}$-spaced signaling at τ seconds. We express the time-domain delay-d MIMO channel matrix as

$$\boldsymbol{H}[d] = \sum_{r=1}^{N_{\rm r}} g_r p\left(dT_{\rm s}-\tau_r\right)\boldsymbol{a}_{\rm r}(\varphi_r)\boldsymbol{a}^*_{\rm t}(\mu_r,\phi_r), \tag{2}$$

where g_r represents the complex path gain of path-r, $\boldsymbol{a}_{\rm r}(\cdot)\in\mathbb{C}^{M_{\rm tot}\times 1}$ and $\boldsymbol{a}_{\rm t}(\cdot,\cdot)\in\mathbb{C}^{N_{\rm tot}\times 1}$ correspond to the receive and transmit array response vectors. The channel frequency response matrix on subcarrier k is the Fourier transform of $\boldsymbol{H}[d]$ such that

$$\boldsymbol{H}[k] = \sum_{r=1}^{N_{\rm r}} g_r\rho_{\tau_r}[k]\boldsymbol{a}_{\rm r}(\varphi_r)\boldsymbol{a}^*_{\rm t}(\mu_r,\phi_r), \tag{3}$$

where $\rho_{\tau_r}[k] = \sum_{d=0}^{D-1} p\left(dT_{\rm s}-\tau_r\right)e^{-{\rm j}\frac{2\pi kd}{N}}$ is the Fourier transform of the delayed sampled filter $p(\tau)$.

Assuming that the UPA employed by the BS is in the xy-plane with $N_{\rm x}$ and $N_{\rm y}$ elements on the x and y axes, then the transmit array response vector is

$$\begin{aligned}\boldsymbol{a}_{\rm t}(\mu_r,\phi_r) = \frac{1}{\sqrt{N_{\rm tot}}}\Big[&1, e^{{\rm j}\frac{2\pi}{\lambda}d_{\rm tx}\sin(\mu_r)\cos(\phi_r)},\cdots,\\ &e^{{\rm j}\frac{2\pi}{\lambda}(N_{\rm x}-1)d_{\rm tx}\sin(\mu_r)\cos(\phi_r)}, e^{{\rm j}\frac{2\pi}{\lambda}d_{\rm ty}\sin(\mu_r)\sin(\phi_r)},\cdots,\\ &e^{{\rm j}\frac{2\pi}{\lambda}((N_{\rm x}-1)d_{\rm tx}\sin(\mu_r)\cos(\phi_r)+(N_{\rm y}-1)d_{\rm ty}\sin(\mu_r)\sin(\phi_r))}\Big]^{\rm T},\end{aligned} \tag{4}$$

where $N_{\rm tot}=N_{\rm x}N_{\rm y}$, λ represents the wavelength corresponding to the operating carrier frequency, $d_{\rm tx}$ and $d_{\rm ty}$ are the inter-element distances of the transmit antenna elements on the x and y axes. Denote by $\theta_r = \frac{2\pi}{\lambda}d_{\rm tx}\sin(\mu_r)\cos(\phi_r)$ and $\psi_r = \frac{2\pi}{\lambda}d_{\rm ty}\sin(\mu_r)\sin(\phi_r)$, which can be interpreted as the elevation and azimuth transmit spatial frequencies for path-r. We further define two vectors $\boldsymbol{a}_{\rm tx}(\theta_r)\in\mathbb{C}^{N_{\rm x}\times 1}$ and $\boldsymbol{a}_{\rm ty}(\psi_r)\in\mathbb{C}^{N_{\rm y}\times 1}$ as

$$\begin{aligned}\boldsymbol{a}_{\rm tx}(\theta_r) &= \tfrac{1}{\sqrt{N_{\rm x}}}\left[1, e^{{\rm j}\theta_r},\cdots,e^{{\rm j}(N_{\rm x}-1)\theta_r}\right]^{\rm T},\\ \boldsymbol{a}_{\rm ty}(\psi_r) &= \tfrac{1}{\sqrt{N_{\rm y}}}\left[1, e^{{\rm j}\psi_r},\cdots,e^{{\rm j}(N_{\rm y}-1)\psi_r}\right]^{\rm T},\end{aligned} \tag{5}$$

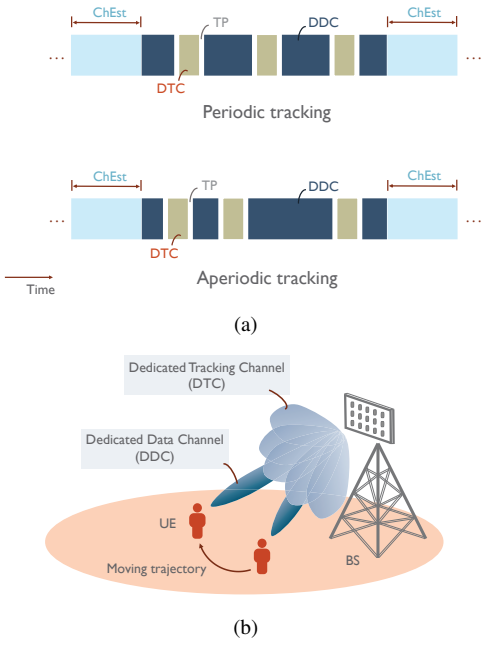

Fig. 2. (a) Potential frame structures of the periodic and aperidoic beam/angle tracking designs. For the periodic beam/angle tracking design, the periodicity of the dedicated tracking channel (DTC) is fixed. For the aperiodic beam/angle tracking design, the DTC is flexibly triggered and configured by the BS. The channel estimation (ChEst), dedicated data channel (DDC) and DTC are multiplexed in the time-domain. A transition period (TP) may exist between the DTC and the DDC. (b) One conceptual example of the multiplexing between the DDC and DTC. The steering directions of the beams in the DDC are adjusted towards the UE's positions, which are obtained via the tracking beams in the DTC.

which can be viewed as the transmit array response vectors in the elevation and azimuth domains. We therefore have $\boldsymbol{a}_{\rm t}(\theta_r,\psi_r)=\boldsymbol{a}_{\rm tx}(\theta_r)\otimes\boldsymbol{a}_{\rm ty}(\psi_r)$ [17]. With this decomposition, we are able to separately track the channel's azimuth and elevation angle information.

Since the ULA is employed by the UE, the receive array response vector is

$$\boldsymbol{a}_{\rm r}(\varphi_r)=\frac{1}{\sqrt{M_{\rm tot}}}\left[1,e^{{\rm j}\frac{2\pi}{\lambda}d_{\rm r}\sin(\varphi_r)},\cdots,e^{{\rm j}\frac{2\pi}{\lambda}d_{\rm r}(M_{\rm tot}-1)\sin(\varphi_r)}\right]^{\rm T},\tag{6}$$

where $d_{\rm r}$ denotes the inter-element distance between the receive antenna elements. Let $\nu_r=\frac{2\pi}{\lambda}d_{\rm r}\sin(\varphi_r)$ denote the receive spatial frequency for path-r. We can rewrite the receive array response vector for the UE as $\boldsymbol{a}_{\rm r}(\nu_r)=\frac{1}{\sqrt{M_{\rm tot}}}\left[1,e^{{\rm j}\nu_r},\cdots,e^{{\rm j}(M_{\rm tot}-1)\nu_r}\right]^{\rm T}$.

C. Frame structure and conventional beam tracking procedures

In Fig. 2(a), we provide a potential frame structure. The time frame consists of three main components: channel estimation (ChEst), dedicated data channel (DDC), and dedicated tracking channel (DTC). The ChEst, DDC and DTC are composed of various numbers of time-slots. Here, we define the time-slot as the basic time unit, which is equivalent to, say, one OFDM symbol duration. We assume a total of T time-slots for one DTC. In the DDC, directional narrow beams are probed by the BS for high-rate data communications, while in the DTC, relatively wide beams are used to track the channel variations. In this paper, the beams in the DTC and the DDC are multiplexed in the time-domain as shown in Fig. 2(a). Further, the beam tracking in the DTC can be conducted in either a periodic or an aperiodic manner as shown in Fig. 2(a). Based on the employed frame structure, we now illustrate the conventional grid-of-beams based beam tracking procedures for mmWave systems.

To reduce the computational complexity and tracking overhead, the beams in the DTC are formed surrounding the beam in the DDC in the angular domain. For simplicity, we first denote the beam in the DDC by anchor beam and the beams in the DTC by backup beams. For a given DTC, the received signal strengths of the anchor and backup beams are measured by the UE and fed back to the BS. If the received signal strength of a backup beam is greater than that of the anchor beam by a certain threshold, the beam training is executed within the probing range of the backup beams to update the steering direction of the anchor beam. Otherwise, the current beam in the DDC is continuously used for data communications until the next DTC is triggered. If the received signal strengths of all the beams in the DTC and DDC are below a given threshold, the complete beam training process as in the channel estimation phase [7], [19] will be conducted.

III. Proposed Angle Tracking Designs for Mobile Wideband mmWave Systems

In this section, we first illustrate the employed beam-specific pilot signal structure for the proposed tracking algorithms. Based on the employed shared-array architecture in Fig. 1, we then explain the design principles of the proposed high-resolution angle tracking approaches assuming the beam-specific pilot signal structure. Further, we present the detailed design procedures for the proposed algorithms along with the discussion of various feedback strategies. Further, we develop both code-division multiplexing (CDM) and time-division multiplexing (TDM) based methods to mitigate the multi-user interference in tracking channels. For practical implementation, we derive the computational complexity and signaling overhead for our proposed algorithms. Unless otherwise specified, we explain the proposed angle tracking strategies in the azimuth domain assuming given elevation AoDs and AoAs. Note that the proposed algorithms can be directly extended to the tracking of the elevation directions.

A. Design principles of proposed angle tracking approaches

The design focus of the proposed angle tracking approaches is to first obtain high-resolution angle estimates, and then track the angle variations via the custom designed tracking beams. We employ the same frame structure as in Fig. 2(a), where the tracking beams are probed during the DTC. In this part, we provide an overview of the auxiliary beam pair-assisted high-resolution angle estimation design for wideband mmWave systems. For simplicity, we focus on the estimation of the azimuth AoDs at the receiver.

$$y[k] = \boldsymbol{a}_{\mathrm{r}}^{*}(\vartheta) g_{r^\star} \rho_{\tau_{r^\star}}[k] \boldsymbol{a}_{\mathrm{r}}(\nu_{r^\star}) \boldsymbol{a}_{\mathrm{t}}^{*}(\theta_{r^\star}, \psi_{r^\star}) \left[\begin{array}{cc} \boldsymbol{a}_{\mathrm{t}}(\eta_{\mathrm{el}}, \eta_{\mathrm{az}} - \delta_{\mathrm{y}}) & \boldsymbol{a}_{\mathrm{t}}(\eta_{\mathrm{el}}, \eta_{\mathrm{az}} + \delta_{\mathrm{y}}) \end{array} \right] \left[\begin{array}{c} s_{i_0}[k] \\ s_{i_1}[k] \end{array} \right]$$
$$\underbrace{+ \boldsymbol{a}_{\mathrm{r}}^{*}(\vartheta) \sum_{\substack{r'=1, \\ r' \neq r^\star}}^{N_{\mathrm{r}}} g_{r'} \rho_{\tau_{r'}}[k] \boldsymbol{a}_{\mathrm{r}}(\nu_{r'}) \boldsymbol{a}_{\mathrm{t}}^{*}(\theta_{r'}, \psi_{r'}) \left[\begin{array}{cc} \boldsymbol{a}_{\mathrm{t}}(\eta_{\mathrm{el}}, \eta_{\mathrm{az}} - \delta_{\mathrm{y}}) & \boldsymbol{a}_{\mathrm{t}}(\eta_{\mathrm{el}}, \eta_{\mathrm{az}} + \delta_{\mathrm{y}}) \end{array} \right] \left[\begin{array}{c} s_{i_0}[k] \\ s_{i_1}[k] \end{array} \right]}_{\text{multi-path interference}}. \tag{10}$$

Each auxiliary beam pair comprises two successively probed analog beams in the angular domain. Pairs of custom designed analog transmit and receive beams are probed to cover the given angular ranges. In this paper, the two analog beams in the same auxiliary beam pair are formed simultaneously by the BS, and are differentiated by the beam-specific pilot signals at the UE side. For instance, to form an azimuth transmit auxiliary beam pair, the two analog beamforming vectors targeted at the directions of $\eta_{\mathrm{az}} - \delta_{\mathrm{y}}$ and $\eta_{\mathrm{az}} + \delta_{\mathrm{y}}$ in the azimuth domain are $\boldsymbol{a}_{\mathrm{t}}(\eta_{\mathrm{el}}, \eta_{\mathrm{az}} - \delta_{\mathrm{y}})$ and $\boldsymbol{a}_{\mathrm{t}}(\eta_{\mathrm{el}}, \eta_{\mathrm{az}} + \delta_{\mathrm{y}})$ respectively, where $\delta_{\mathrm{y}} = \frac{2\ell_{\mathrm{y}}\pi}{N_{\mathrm{y}}}$ with $\ell_{\mathrm{y}} = 1, \cdots, \frac{N_{\mathrm{y}}}{4}$ and η_{el} corresponds to a given elevation direction. Now, we illustrate the employed pilot signal structure.

Due to the constant amplitude and the robustness to the frequency selectivity, Zadoff-Chu (ZC)-type sequences are used in this paper as the pilot signals for tracking. Denoting the sequence length by N_{ZC}, the employed ZC sequence with root index i_z is

$$s_{i_z}[m] = \exp\left(-\mathrm{j}\frac{\pi m(m+1) i_z}{N_{\mathrm{ZC}}}\right), \tag{7}$$

where $m = 0, \cdots, N_{\mathrm{ZC}} - 1$. Here, we let $N_{\mathrm{ZC}} = N$ (i.e., the total number of employed subcarriers) and $z = 0, 1$ such that i_0 and i_1 correspond to the two beams in the same auxiliary beam pair. By cross correlating two ZC sequences at zero-lag, we can obtain [21]

$$\sum_{k=0}^{N-1} s_{i_0}[k] s_{i_1}^{*}[k] = \begin{cases} 1, & \text{if } i_0 = i_1 \\ \beta_{i_0,i_1}, & \text{otherwise.} \end{cases} \tag{8}$$

Here, β_{i_0,i_1} is a constant, corresponding to $1/\sqrt{N_{\mathrm{ZC}}}$. For relatively large sequence length N_{ZC}, $|\beta_{i_0,i_1}| \approx 0$. In this paper, we assume $\beta_{i_0,i_1} = 0$ for better illustration of the proposed methods. For a relatively small sequence length N_{ZC}, this approximated code-domain orthogonality condition may not hold, resulting in significant inter-beam interference. To counter this challenge, the BS can probe the two beams in the same auxiliary beam pair in a round-robin TDM manner. In contrast to simultaneous probing, the TDM approach can eliminate the inter-beam interference, but may introduce extra access delay to the system. Note that the selection of appropriate sequence length N_{ZC} also depends on the channel condition, which will be elaborated later in this section. In practical systems, the RF impairments such as the I/Q imbalance and power amplifier nonlinearities would distort the received ZC sequence samples, resulting in degraded correlation performance. In this paper, we ignore these impairments in the employed system model as they do not affect the key design principles of our proposed tracking strategies.

Based on the employed pilot signal structure, we now explain the design principles of the auxiliary beam pair-assisted angle acquisition. Assume $M_{\mathrm{RF}} = 1$ and a given analog receive beam, say, $\boldsymbol{a}_{\mathrm{r}}(\vartheta)$. According to the employed array configurations and the pilot signal structure, we can then rewrite (1) in the absence of noise as

$$\begin{aligned} y[k] =& \boldsymbol{a}_{\mathrm{r}}^{*}(\vartheta) \sum_{r=1}^{N_{\mathrm{r}}} g_r \rho_{\tau_r}[k] \boldsymbol{a}_{\mathrm{r}}(\nu_r) \boldsymbol{a}_{\mathrm{t}}^{*}(\theta_r, \psi_r) \\ & \times \left[\begin{array}{cc} \boldsymbol{a}_{\mathrm{t}}(\eta_{\mathrm{el}}, \eta_{\mathrm{az}} - \delta_{\mathrm{y}}) & \boldsymbol{a}_{\mathrm{t}}(\eta_{\mathrm{el}}, \eta_{\mathrm{az}} + \delta_{\mathrm{y}}) \end{array} \right] \\ & \times \left[\begin{array}{c} s_{i_0}[k] \\ s_{i_1}[k] \end{array} \right]. \end{aligned} \tag{9}$$

Our design focus here is to estimate the azimuth transmit spatial frequency $\psi_{r^\star}$ for path-$r^\star$ with $r^\star \in \{1, \cdots, N_{\mathrm{r}}\}$. We first assume that $\psi_{r^\star}$ falls into the probing range of the auxiliary beam pair such that $\psi_{r^\star} \in (\eta_{\mathrm{az}} - \delta_{\mathrm{y}}, \eta_{\mathrm{az}} + \delta_{\mathrm{y}})$. We can then rewrite (9) to obtain (10). In this paper, we focus on tracking the variations of the steering angle of the data beam, which is $\psi_{r^\star}$ in this example. To reduce the implementation complexity and improve the tracking accuracy, narrow tracking beams are formed, closely surrounding the steering angle of the data beam. The resulted effective beam-space channels therefore contain few paths/clusters, though the general mmWave channels may have many rays in the entire angular domain according to the channel modeling progress in 3GPP [22] and channel measurement campaigns [23], [24]. For instance, denote the angular coverage of the auxiliary beam pair $\{\boldsymbol{a}_{\mathrm{t}}(\eta_{\mathrm{el}}, \eta_{\mathrm{az}} - \delta_{\mathrm{y}}), \boldsymbol{a}_{\mathrm{t}}(\eta_{\mathrm{el}}, \eta_{\mathrm{az}} + \delta_{\mathrm{y}})\}$ in (10) by Ξ_{y}. For relatively large number of transmit antennas, it becomes highly likely that only the steering angle of the data beam, i.e., $\psi_{r^\star}$ is within Ξ_{y}, and other paths' spatial frequencies $\psi_{r'} \notin \Xi_{\mathrm{y}}$ for $r' \in \{1, \cdots, N_{\mathrm{r}}\}$ and $r' \neq r^\star$. In this case, the multi-path interference would become negligible, and the received signal in (10) can be approximated to

$$\begin{aligned} y[k] \approx& g_{r^\star} \rho_{\tau_{r^\star}}[k] \boldsymbol{a}_{\mathrm{r}}^{*}(\vartheta) \boldsymbol{a}_{\mathrm{r}}(\nu_{r^\star}) \boldsymbol{a}_{\mathrm{t}}^{*}(\theta_{r^\star}, \psi_{r^\star}) \\ & \times \left[\begin{array}{cc} \boldsymbol{a}_{\mathrm{t}}(\eta_{\mathrm{el}}, \eta_{\mathrm{az}} - \delta_{\mathrm{y}}) & \boldsymbol{a}_{\mathrm{t}}(\eta_{\mathrm{el}}, \eta_{\mathrm{az}} + \delta_{\mathrm{y}}) \end{array} \right] \\ & \times \left[\begin{array}{c} s_{i_0}[k] \\ s_{i_1}[k] \end{array} \right]. \end{aligned} \tag{11}$$

Note that we can extend the algorithm to separately estimate multiple paths in parallel.

Assuming perfect time-frequency synchronization, the UE employs locally stored reference beam-specific sequences to correlate the received signal samples. By using the reference

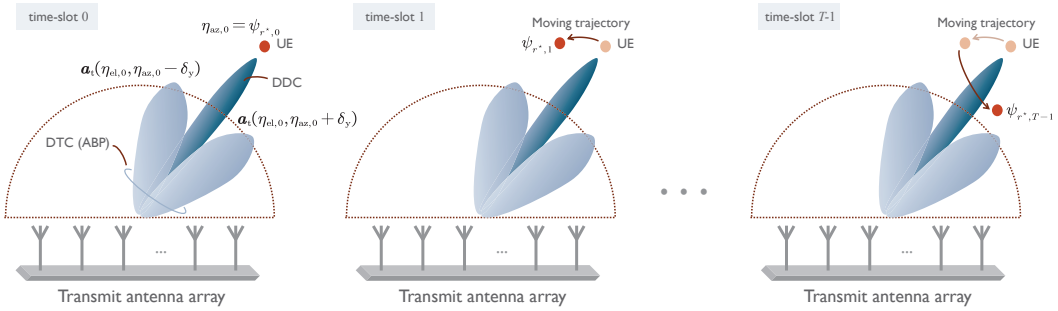

Fig. 3. Conceptual examples of the relationship between the UE's moving trajectory (i.e., the angle variations) and the auxiliary beam pair based tracking beams in the DTC. As long as the relative position of the UE to the transmit antenna array is within the probing range of the auxiliary beam pair, it is expected to be tracked via the tracking beams in the DTC.

ZC sequence with the sequence root index i_0, we can first obtain

$$\begin{aligned}\Lambda_{\text{az}}^{\Delta} &= \sum_{k=0}^{N-1} s_{i_0}^*[k]y[k] \qquad (12)\\ &= \sum_{k=0}^{N-1} \big(g_{r^\star}\rho_{\tau_{r^\star}}[k]\boldsymbol{a}_{\text{r}}^*(\vartheta)\boldsymbol{a}_{\text{r}}(\nu_{r^\star})\boldsymbol{a}_{\text{t}}^*(\theta_{r^\star},\psi_{r^\star})\\ &\quad\times \boldsymbol{a}_{\text{t}}(\eta_{\text{el}},\eta_{\text{az}}-\delta_{\text{y}})s_{i_0}^*[k]s_{i_0}[k]\big)\\ &\quad+\sum_{k=0}^{N-1}\big(g_{r^\star}\rho_{\tau_{r^\star}}[k]\boldsymbol{a}_{\text{r}}^*(\vartheta)\boldsymbol{a}_{\text{r}}(\nu_{r^\star})\boldsymbol{a}_{\text{t}}^*(\theta_{r^\star},\psi_{r^\star})\\ &\quad\times \boldsymbol{a}_{\text{t}}(\eta_{\text{el}},\eta_{\text{az}}+\delta_{\text{y}})s_{i_0}^*[k]s_{i_1}[k]\big). \qquad (13)\end{aligned}$$

We assume flat channels here such that $\bar{\rho}_{\tau_{r^\star}}=\rho_{\tau_{r^\star}}[0]=\cdots=\rho_{\tau_{r^\star}}[N-1]$ for better illustration of the design principles. The proposed design approach can still achieve promising angle estimation/tracking performance in wideband channels (verified in Section V-C) since the correlation properties of the ZC-type sequences are robust to the frequency selectivity (e.g., up to 8.6 MHz continuous bandwidth in LTE [25]). We can then rewrite (13) as

$$\begin{aligned}\Lambda_{\text{az}}^{\Delta} =& g_{r^\star}\boldsymbol{a}_{\text{r}}^*(\vartheta)\boldsymbol{a}_{\text{r}}(\nu_{r^\star})\boldsymbol{a}_{\text{t}}^*(\theta_{r^\star},\psi_{r^\star})\boldsymbol{a}_{\text{t}}(\eta_{\text{el}},\eta_{\text{az}}-\delta_{\text{y}})\\ &\times\bar{\rho}_{\tau_{r^\star}}\sum_{k=0}^{N-1}s_{i_0}^*[k]s_{i_0}[k]\\ &+g_{r^\star}\boldsymbol{a}_{\text{r}}^*(\vartheta)\boldsymbol{a}_{\text{r}}(\nu_{r^\star})\boldsymbol{a}_{\text{t}}^*(\theta_{r^\star},\psi_{r^\star})\boldsymbol{a}_{\text{t}}(\eta_{\text{el}},\eta_{\text{az}}+\delta_{\text{y}})\\ &\times\bar{\rho}_{\tau_{r^\star}}\sum_{k=0}^{N-1}s_{i_0}^*[k]s_{i_1}[k] \qquad (14)\\ \overset{(a)}{=}& g_{r^\star}\bar{\rho}_{\tau_{r^\star}}\boldsymbol{a}_{\text{r}}^*(\vartheta)\boldsymbol{a}_{\text{r}}(\nu_{r^\star})\boldsymbol{a}_{\text{t}}^*(\theta_{r^\star},\psi_{r^\star})\boldsymbol{a}_{\text{t}}(\eta_{\text{el}},\eta_{\text{az}}-\delta_{\text{y}}), \qquad (15)\end{aligned}$$

where (a) is due to the employed beam-specific pilot signal structure in (8). We then compute the corresponding received signal strength as $\chi_{\text{az}}^{\Delta}=\left(\Lambda_{\text{az}}^{\Delta}\right)^*\Lambda_{\text{az}}^{\Delta}$. Similarly, using the ZC sequence with the root index i_1 to correlate the received signal samples, we obtain

$$\begin{aligned}\Lambda_{\text{az}}^{\Sigma} &= \sum_{k=0}^{N-1}s_{i_1}^*[k]y[k]\\ &= g_{r^\star}\bar{\rho}_{\tau_{r^\star}}\boldsymbol{a}_{\text{r}}^*(\vartheta)\boldsymbol{a}_{\text{r}}(\nu_{r^\star})\boldsymbol{a}_{\text{t}}^*(\theta_{r^\star},\psi_{r^\star})\boldsymbol{a}_{\text{t}}(\eta_{\text{el}},\eta_{\text{az}}+\delta_{\text{y}}). \qquad (16)\end{aligned}$$

We can calculate the corresponding received signal strength as $\chi_{\text{az}}^{\Sigma}=\left(\Lambda_{\text{az}}^{\Sigma}\right)^*\Lambda_{\text{az}}^{\Sigma}$. We define the ratio metric as $\zeta_{\text{az}}=(\chi_{\text{az}}^{\Delta}-\chi_{\text{az}}^{\Sigma})/(\chi_{\text{az}}^{\Delta}+\chi_{\text{az}}^{\Sigma})$. According to [16, Lemma 1], if $|\psi_{r^\star}-\eta_{\text{az}}|<\delta_{\text{y}}$, then the azimuth transmit spatial frequency $\psi_{r^\star}$ is within the range of $(\eta_{\text{az}}-\delta_{\text{y}},\eta_{\text{az}}+\delta_{\text{y}})$, and ζ_{az} is a monotonically decreasing function of $\psi_{r^\star}-\eta_{\text{az}}$ and invertible with respect to $\psi_{r^\star}-\eta_{\text{az}}$. Via the inverse function, we can therefore derive the estimated value of $\psi_{r^\star}$ as

$$\begin{aligned}\hat{\psi}_{r^\star} &= \eta_{\text{az}}\\ &\quad-\arcsin\left(\frac{\zeta_{\text{az}}\sin(\delta_{\text{y}})-\zeta_{\text{az}}\sqrt{1-\zeta_{\text{az}}^2}\sin(\delta_{\text{y}})\cos(\delta_{\text{y}})}{\sin^2(\delta_{\text{y}})+\zeta_{\text{az}}^2\cos^2(\delta_{\text{y}})}\right). \qquad (17)\end{aligned}$$

If ζ_{az} is perfect, i.e., not impaired by noise and other types of interference, we can perfectly recover the azimuth transmit spatial frequency for path-$r^\star$, i.e., $\psi_{r^\star}=\hat{\psi}_{r^\star}$.

In Section III-B, we restrict to the tracking of path-$r^\star$'s azimuth AoD. To better reveal the temporal evolution, we use $\psi_{r^\star,t}$ instead of $\psi_{r^\star}$ to represent path-$r^\star$'s azimuth transmit spatial frequency for a given time-slot $t\in\{0,\cdots,T-1\}$ in the DTC.

B. Design procedures of proposed angle tracking approaches

Leveraging the high-resolution angle estimates, we exploit the auxiliary beam pair design in forming tracking beams in the DTC. For example, we assume that one transmit auxiliary beam pair (e.g., $\boldsymbol{a}_{\text{t}}(\eta_{\text{el}},\eta_{\text{az}}-\delta_{\text{y}})$ and $\boldsymbol{a}_{\text{t}}(\eta_{\text{el}},\eta_{\text{az}}+\delta_{\text{y}})$) is probed during the DTC. The boresight angle of the auxiliary beam pair (e.g., η_{az}) is identical to the steering direction of the corresponding anchor beam in the DDC. In the following, we first illustrate the general framework of the proposed angle tracking designs.

In Fig. 3, we provide the relationship between the UE's moving trajectory and the tracking beams in the DTC. At time-slot 0, the anchor beam in the DDC with the azimuth boresight angle $\eta_{\text{az},0}$ steers towards the UE of interest. One azimuth transmit auxiliary beam pair is formed as the tracking beams in the DTC. For a given elevation direction $\eta_{\text{el},0}$, the corresponding two beams probe towards $\eta_{\text{az},0}-\delta_{\text{y}}$ and

$\eta_{\mathrm{az},0} + \delta_{\mathrm{y}}$ with the boresight angle $\eta_{\mathrm{az},0}$ in the azimuth domain. As can be seen from the conceptual example shown in Fig. 3, at time-slots $1, \cdots, T-1$, the UE of interest moves away from the original azimuth position $\psi_{r^\star,0}$ (or $\eta_{\mathrm{az},0}$) to $\psi_{r^\star,1}, \cdots, \psi_{r^\star,T-1}$. Note that as long as $\psi_{r^\star,1}, \cdots, \psi_{r^\star,T-1}$ are in the probing range of the tracking beams, they are expected to be accurately tracked according to the design principles of the auxiliary beam pair.

In the proposed methods, either the BS or the UE can trigger the angle tracking process, which are referred to as BS-driven or UE-driven angle tracking methods. For both the BS-driven and UE-driven angle tracking strategies, either a periodic or aperiodic DTC design can be adopted. Further, for the proposed BS-driven angle tracking, no prior knowledge of the auxiliary beam pair setup is required at the UE side. In the following two parts, we first present the detailed design procedures of the proposed methods and illustrate the employed direct and differential feedback strategies; we then develop potential solutions to reduce the multi-user interference in tracking channels.

1. BS/UE-driven angle tracking design with direct/differential ratio metric feedback. We start by illustrating the BS-driven angle tracking strategy using the direct ratio metric feedback. For a given time-slot $t \in \{0, \cdots, T-1\}$ in the DTC, the corresponding ratio metric $\zeta_{\mathrm{az},t}$ is calculated by the UE using the probed azimuth transmit auxiliary beam pair. First, assume that the BS triggers the feedback of the derived ratio metric. For instance, considering a given DTC, if the BS requires the ratio metric feedback at time-slot $T-1$, $\zeta_{\mathrm{az},T-1}$ is then quantized and sent back to the BS. In this case, time-slot $T-1$ is the last time-slot of a given DTC. Note that in practice, the BS may require the ratio metric feedback for multiple time-slots within the same DTC to track the fast-varying channels. It is therefore essential for the UE to keep computing the ratio metric for every time-slot in the DTC. Upon receiving the ratio metric feedback from the UE at time-slot t, the BS retrieves the corresponding angle estimate according to (17). Denoting the azimuth angle estimate at time-slot t by $\hat{\psi}_{r^\star,t}$, we have

$$\hat{\psi}_{r^\star,t} = \eta_{\mathrm{az},0} - \arcsin\left(\frac{\zeta_{\mathrm{az},t}\sin(\delta_{\mathrm{y}})}{\sin^2(\delta_{\mathrm{y}}) + \zeta_{\mathrm{az},t}^2\cos^2(\delta_{\mathrm{y}})} - \frac{\zeta_{\mathrm{az},t}\sqrt{1-\zeta_{\mathrm{az},t}^2}\sin(\delta_{\mathrm{y}})\cos(\delta_{\mathrm{y}})}{\sin^2(\delta_{\mathrm{y}}) + \zeta_{\mathrm{az},t}^2\cos^2(\delta_{\mathrm{y}})}\right). \quad (18)$$

The angle difference $\Delta\psi_{r^\star,t} = \left|\psi_{r^\star,0} - \hat{\psi}_{r^\star,t}\right|$ is then calculated by the BS and compared with a predefined threshold ς_{az}. If $\Delta\psi_{r^\star,t} \geq \varsigma_{\mathrm{az}}$, the azimuth steering direction of the anchor beam in the DDC is then updated from $\eta_{\mathrm{az},0}$ to $\eta_{\mathrm{az},t} = \hat{\psi}_{r^\star,t}$. Otherwise, the azimuth steering direction of the anchor beam in the DDC is kept unchanged from time-slot 0, i.e., $\eta_{\mathrm{az},t} = \eta_{\mathrm{az},0}$.

Different from the BS-driven strategy, the angle tracking process in the UE-driven method is triggered at the UE side. Here, the direct ratio metric feedback is still applied, but the feedback process is configured by the UE according to the received signal strength corresponding to the anchor beam in the DDC. We explain the design procedures of the UE-driven angle tracking approach with the direct ratio metric feedback in Algorithm 1. Note that in the proposed UE-driven angle tracking with the direct ratio metric feedback, no prior knowledge of the auxiliary beam pair setup is required at the UE side, while only the received signal strength of the anchor beam is deduced as the triggering performance metric. By exploiting the symmetric property of the ratio metric [17], the BS-driven and UE-driven differential ratio metric feedback strategies can be similarly derived relative to the direct ratio metric feedback designs with moderate modifications on the tracking procedures.

Algorithm 1 UE-driven angle tracking design with direct feedback of the ratio metric

BS-side processing

1: For $t \in \{0, \cdots, T-1\}$, the BS probes the auxiliary beam pair(s) for angle tracking.

UE-side processing

2: The UE calculates the ratio metric $\zeta_{\mathrm{az},t}$, the received signal strengths γ_t and γ_0 of the DDCs at time-slots t and 0, and $\Delta\gamma_t = \gamma_t - \gamma_0$.

3: **If** $\Delta\gamma_t \geq \varrho_{\mathrm{az}}$

4: The UE quantizes $\zeta_{\mathrm{az},t}$ and sends it back to the BS.

5: **Else**

6: Start from step-1 for time-slot $t+1$.

7: **end If**

BS-side processing

8: The BS retrieves the channel's azimuth transmit spatial frequency $\hat{\psi}_{r^\star,t}$ according to (18).

9: The BS updates the azimuth steering direction of the data beam as $\eta_{\mathrm{az},t} = \hat{\psi}_{r^\star,t}$.

Remark: Similar to the direct and differential ratio metric feedback methods, direct and differential angle feedback strategies can also be supported for the angle tracking designs, as long as necessary auxiliary beam pair setup is available at the UE side.

To compensate for the noise and other types of impairments, we can also form multiple identical auxiliary beam pairs to track a given angle's variations if the angle tracking is triggered. Upon receiving all the pilot signal samples, the UE can either average the received signal strengths or select the highest received signal strengths across all probings to derive the corresponding ratio metric. By exploiting this spreading gain from multiple probings/snapshots of the auxiliary beam pairs, we expect to improve the angle tracking performance especially with low SNR and high multi-path interference.

2. Multi-user interference between dedicated tracking channels (DTCs). Having dedicated RFs for tracking reduces the spatial degrees-of-freedom (DoFs) to mitigate the multi-user interference (MUI) when different UEs share the same time and frequency resources. We consider a multi-user scenario, in which all UEs of interest are conducting angle tracking via the corresponding auxiliary beam pairs (dedicated tracking channels). We provide one conceptual example in Fig. 4 to characterize this interference scenario and explain our

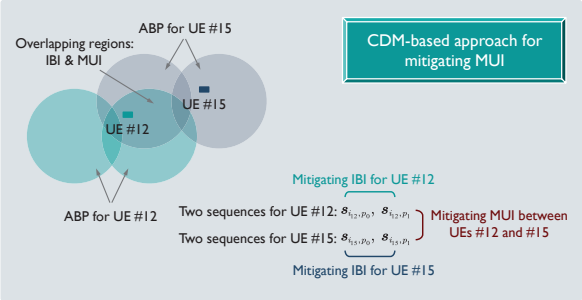

(a)

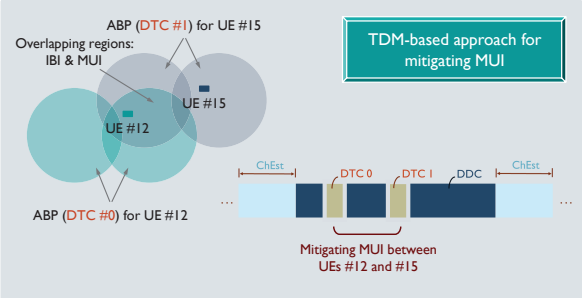

(b)

Fig. 4. Bird's-eye view of the multi-user interference (MUI) between the DTCs and potential solutions. (a) CDM based multi-user interference mitigation strategy. (b) TDM based multi-user interference mitigation strategy.

proposed solutions. As can be seen from Fig. 4, if the UEs of interest are close to each other such that they are within the probing ranges of each other's auxiliary beam pairs, they would significantly interfere with each other if the same time-frequency resources are occupied and identical sequences are used. To mitigate the interference, we propose CDM and/or TDM based design approaches. We do not focus on frequency-division multiplexing (FDM) based strategy as the tracking beams are wideband and applied to all active subcarriers.

For CDM based design option, all simultaneously probed beams targeting for different UEs can embed distinct ZC sequences with different root indices. The number of such sequences, however, may not be enough to support a relatively large number of UEs in the network. To counter this problem, we develop an alternative CDM based approach by leveraging a custom designed hierarchical sequence structure. Here, we still employ the ZC-type sequences, and express the sequence structure as

$$s_{i_u,p_z}[m] = \exp\left(-\mathrm{j}\frac{\pi(m+p_z)(m+p_z+1)i_u}{N_{\mathrm{ZC}}}\right), \quad (19)$$

where $m = 0, \cdots, N_{\mathrm{ZC}}-1$, i_u denotes the root index associated with a specific auxiliary beam pair that serves UE u, and p_z's ($z = 0, 1$) represent the circular shifts in the frequency domain, corresponding to the two beams in the same auxiliary beam pair. For instance, in Fig. 4(a), the BS transmits the hierarchical sequences to the two UEs with the user indices, say #12 and #15 via the corresponding two auxiliary beam pairs. Assuming perfect time-frequency synchronization, UE #12 applies locally stored sequences $\boldsymbol{s}_{i_{12},p_0} = \{s_{i_{12},p_0}[0], \cdots, s_{i_{12},p_0}[N_{\mathrm{ZC}}-1]\}$ and $\boldsymbol{s}_{i_{12},p_1} = \{s_{i_{12},p_1}[0], \cdots, s_{i_{12},p_1}[N_{\mathrm{ZC}}-1]\}$ to correlate the received signal samples and to derive the corresponding ratio metric. Similarly, UE #15 employs $\boldsymbol{s}_{i_{15},p_0} = \{s_{i_{15},p_0}[0], \cdots, s_{i_{15},p_0}[N_{\mathrm{ZC}}-1]\}$ and $\boldsymbol{s}_{i_{15},p_1} = \{s_{i_{15},p_1}[0], \cdots, s_{i_{15},p_1}[N_{\mathrm{ZC}}-1]\}$ to correlate the received signal samples. According to (8), the cross-correlation interference between UEs #12 and #15 can be minimized by choosing appropriate sequence length N_{ZC} and root indices i_{12} and i_{15}. For a given UE, the inter-beam interference (IBI) is subject to the correlation of two cyclically shifted ZC sequences with the same root index. This correlation is zero without incorporating noise and other impairments, but in practice it is subject to the maximum delay spread and Doppler shift of the channels [26].

In addition to the proposed CDM based design strategy, the MUI can also be mitigated if the BS performs angle tracking for different UEs in a TDM manner. We employ the example shown in Fig. 4(b) to illustrate the procedures. As can be seen from Fig. 4(b), the BS employs different time-slots to steer the auxiliary beam pairs towards UEs #12 and #15 for angle tracking. Obviously, there would be no interference between UE #12 and UE #15. The TDM strategy, however, would introduce extra access delay to the network in contrast to the code-domain approaches. For practical implementation, a hybrid approach of both CDM and TDM based strategies would be of design interest to mitigate the interference.

C. Computational complexity and signaling overhead

In this part, we first evaluate the implementation complexity of the proposed angle tracking algorithms. As the angle tracking does not involve extensive beam search as in the angle estimation phase, we focus on the number of complex arithmetic operations required at the UE. The complex arithmetic operation includes complex multiplication, division, addition and substraction. In the proposed angle tracking methods, the complex arithmetic operations are mainly resulted from correlating the received signal samples with reference ZC sequences. For a length-N_{ZC} ZC sequence, the number of complex arithmetic operations required to perform the zero-lag correlation is $2N_{\mathrm{ZC}}-1$. If a total of N_{ABP} auxiliary beam pairs are probed (we set $N_{\mathrm{ABP}} = 1$ when deriving the design principles and procedures) in a DTC to enhance the angular coverage, this number becomes $2N_{\mathrm{ABP}}(2N_{\mathrm{ZC}}-1)$. Further, assuming that a total of N_{DTC} DTCs are triggered for angle tracking, the number of complex arithmetic operations is $2N_{\mathrm{DTC}}N_{\mathrm{ABP}}(2N_{\mathrm{ZC}}-1)$.

In this paper, we characterize the signaling overhead for tracking as the ratio between the number of OFDM symbols used for the DTCs (M_{DTC}) and the total number of symbols (M_{TOT}). We first assume that the beams in the auxiliary beam pairs are probed in the TDM manner. For a total of M_{ABP} auxiliary beam pairs, we can obtain $M_{\mathrm{DTC}} = 2M_{\mathrm{ABP}}$. We can then compute the corresponding overhead ratio as $2M_{\mathrm{ABP}}/M_{\mathrm{TOT}}$. For the CDM based design strategy, we have $M_{\mathrm{DTC}} = M_{\mathrm{ABP}}/N_{\mathrm{ABP}}$, recalling that N_{ABP} is the number of simultaneously probed auxiliary beam pairs during one DTC. In this case, we can derive the ratio as $M_{\mathrm{ABP}}/N_{\mathrm{ABP}}M_{\mathrm{TOT}}$.

Obviously, the CDM based method requires less signaling overhead than the TDM based strategy assuming the same M_{ABP}, but its tracking performance is subject to the inter-beam interference. For instance, if $M_{\mathrm{TOT}} = 10^4$, $M_{\mathrm{ABP}} = 100$ and $N_{\mathrm{ABP}} = 1$, we can compute the corresponding signaling overhead as 1% for the CDM based design approach. This signaling overhead is similar to the frame timing synchronization design in LTE systems [25], in which one out of 70 OFDM symbols with normal CP length is used to carry the corresponding synchronization signal (1.4%). This 1% signaling overhead for tracking is equivalent to $\rho = 1\%$ assumed in the simulation section, which shows promising angle tracking performances under various deployment scenarios.

IV. Impact of Radiation Pattern Impairments

Because of manufacturing inaccuracies, a variety of impairments such as geometrical and electrical tolerances cause non-uniform amplitude and phase characteristics of the individual antenna elements [27]. This results in phase and amplitude errors of the radiation patterns [28]. The angle tracking performance of the proposed auxiliary beam pair-assisted designs is subject to the radiation pattern impairments, which are neglected during the derivation of the ratio metric. If the radiation patterns of the beams in the auxiliary beam pair are impaired by the phase and amplitude errors, the monotonic and symmetric properties of the ratio metric may not hold, which in turn, results in large angle tracking errors. In the following, we first illustrate the impact of the radiation pattern impairments on the proposed angle tracking designs. To calibrate the antenna array with the analog architecture, we custom design and evaluate an array calibration method. We then examine the impact of the residual calibration errors on the proposed angle tracking approaches.

A. Impact of phase and amplitude errors on proposed methods

Neglecting mutual coupling and matching effects, and denoting the phase and amplitude error matrices by $\boldsymbol{P}$ and $\boldsymbol{A}$, we have $\boldsymbol{P} = \mathrm{diag}([e^{\mathrm{j}p_0}, e^{\mathrm{j}p_1}, \cdots, e^{\mathrm{j}p_{N_{\mathrm{tot}}-1}}]^{\mathrm{T}})$ and $\boldsymbol{A} = \mathrm{diag}([a_0, a_1, \cdots, a_{N_{\mathrm{tot}}-1}]^{\mathrm{T}})$, where p_i and a_i correspond to the phase and amplitude errors on the i-th antenna element with $i = 0, \cdots, N_{\mathrm{tot}} - 1$. Due to the UPA structure, we can decompose $\boldsymbol{P}$ and $\boldsymbol{A}$ as $\boldsymbol{P} = \boldsymbol{P}_{\mathrm{el}} \otimes \boldsymbol{P}_{\mathrm{az}}$ and $\boldsymbol{A} = \boldsymbol{A}_{\mathrm{el}} \otimes \boldsymbol{A}_{\mathrm{az}}$, where $\boldsymbol{P}_{\mathrm{el}} = \mathrm{diag}([e^{\mathrm{j}p_{\mathrm{el},0}}, e^{\mathrm{j}p_{\mathrm{el},1}}, \cdots, e^{\mathrm{j}p_{\mathrm{el},N_{\mathrm{x}}-1}}]^{\mathrm{T}})$ and $\boldsymbol{A}_{\mathrm{el}} = \mathrm{diag}([a_{\mathrm{el},0}, a_{\mathrm{el},1}, \cdots, a_{\mathrm{el},N_{\mathrm{x}}-1}]^{\mathrm{T}})$ correspond to the elevation domain, and $\boldsymbol{P}_{\mathrm{az}} = \mathrm{diag}([e^{\mathrm{j}p_{\mathrm{az},0}}, e^{\mathrm{j}p_{\mathrm{az},1}}, \cdots, e^{\mathrm{j}p_{\mathrm{az},N_{\mathrm{y}}-1}}]^{\mathrm{T}})$ and $\boldsymbol{A}_{\mathrm{az}} = \mathrm{diag}([a_{\mathrm{az},0}, a_{\mathrm{az},1}, \cdots, a_{\mathrm{az},N_{\mathrm{y}}-1}]^{\mathrm{T}})$ are for the azimuth domain. In this paper, we model $p_{\mathrm{el},i_{\mathrm{el}}}$, $a_{\mathrm{el},i_{\mathrm{el}}}$ with $i_{\mathrm{el}} = 0, \cdots, N_{\mathrm{x}} - 1$ and $p_{\mathrm{az},i_{\mathrm{az}}}$, $a_{\mathrm{az},i_{\mathrm{az}}}$ with $i_{\mathrm{az}} = 0, \cdots, N_{\mathrm{y}} - 1$ as Gaussian distributed random variables with zero mean and certain variances. Note that other distributions of phase and amplitude errors are possible depending on array geometry, array size, and other array configurations. Our proposed array calibration strategy does not rely on specific phase and amplitude errors distributions. Further, the proposed calibration method is performed off-line assuming time-invariant phase and amplitude errors. If the phase and amplitude errors slowly change over time, we can still apply the proposed off-line calibration method in a semi-static manner. If the phase and amplitude errors dynamically evolve over time, on-line array calibration methods are needed to frequently compensate for the phase and amplitude impairments in seconds, which are beyond the scope of this paper.

We employ the beam pair example discussed in Section III-A to illustrate the impact of the phase and amplitude errors on the auxiliary beam pair design. Denote $\boldsymbol{C} = \boldsymbol{A}\boldsymbol{P}$ and neglect the radiation pattern impairments at the UE side. Using the transmit analog beam $\boldsymbol{a}_{\mathrm{t}}(\eta_{\mathrm{el}}, \eta_{\mathrm{az}} - \delta_{\mathrm{y}})$ and the receive analog beam $\boldsymbol{a}_{\mathrm{r}}(\vartheta)$, we compute the corresponding noiseless received signal strength as

$$\begin{aligned}\chi_{\mathrm{az}}^{\Delta} &= |g_{r^\star}\bar{\rho}_{\tau_{r^\star}}|^2 \, |\boldsymbol{a}_{\mathrm{r}}^*(\vartheta)\boldsymbol{a}_{\mathrm{r}}(\nu_{r^\star})|^2 \\ &\quad \times \boldsymbol{a}_{\mathrm{t}}^*(\eta_{\mathrm{el}}, \eta_{\mathrm{az}} - \delta_{\mathrm{y}})\boldsymbol{C}^*\boldsymbol{a}_{\mathrm{t}}(\theta_{r^\star}, \psi_{r^\star}) \\ &\quad \times \boldsymbol{a}_{\mathrm{t}}^*(\theta_{r^\star}, \psi_{r^\star})\boldsymbol{C}\boldsymbol{a}_{\mathrm{t}}(\eta_{\mathrm{el}}, \eta_{\mathrm{az}} - \delta_{\mathrm{y}}) \qquad (20) \\ &= |g_{r^\star}\bar{\rho}_{\tau_{r^\star}}|^2 \, |\boldsymbol{a}_{\mathrm{r}}^*(\vartheta)\boldsymbol{a}_{\mathrm{r}}(\nu_{r^\star})|^2 \\ &\quad \times \left| \sum_{i_{\mathrm{el}}=0}^{N_{\mathrm{x}}-1} a_{\mathrm{el},i_{\mathrm{el}}} e^{-\mathrm{j}\left[i_{\mathrm{el}}(\theta_{r^\star} - \eta_{\mathrm{el}}) - p_{\mathrm{el},i_{\mathrm{el}}}\right]} \right|^2 \\ &\quad \times \left| \sum_{i_{\mathrm{az}}=0}^{N_{\mathrm{y}}-1} a_{\mathrm{az},i_{\mathrm{az}}} e^{-\mathrm{j}[i_{\mathrm{az}}(\psi_{r^\star} - \eta_{\mathrm{az}} + \delta_{\mathrm{y}}) - p_{\mathrm{az},i_{\mathrm{az}}}]} \right|^2 . \qquad (21)\end{aligned}$$

We can similarly obtain the received signal strength $\chi_{\mathrm{az}}^{\Sigma}$ with respect to the transmit and receive beams pair $\boldsymbol{a}_{\mathrm{t}}(\eta_{\mathrm{el}}, \eta_{\mathrm{az}} + \delta_{\mathrm{y}})$ and $\boldsymbol{a}_{\mathrm{r}}(\vartheta)$. Due to the phase and amplitude errors, the ratio metric calculated via $\zeta_{\mathrm{az}} = \frac{\chi_{\mathrm{az}}^{\Delta} - \chi_{\mathrm{az}}^{\Sigma}}{\chi_{\mathrm{az}}^{\Delta} + \chi_{\mathrm{az}}^{\Sigma}}$ is therefore no longer a strict monotonic function of the angle to be estimated. By directly inverting the ratio metric function as according to (17), high angle estimation error probability could be incurred, which in turn, degrades the angle tracking performance of the proposed methods.

In Figs. 5(a) and 5(b), we plot the azimuth radiation patterns with and without phase and amplitude errors for comparison. For a given ψ_0, we calculate $\left|\boldsymbol{a}_{\mathrm{ty}}^*(\psi)\boldsymbol{D}^*\boldsymbol{a}_{\mathrm{ty}}(\psi_0)\right|^2$ as a sample point corresponding to $\psi \in [-\pi/2, \pi/2]$, where $\boldsymbol{D} = \boldsymbol{I}_{N_{\mathrm{y}}}$ assuming no phase and amplitude errors, and $\boldsymbol{D} = \boldsymbol{A}_{\mathrm{az}}\boldsymbol{P}_{\mathrm{az}}$ assuming both phase and amplitude errors for the azimuth domain. We then form the radiation pattern by collecting all the sample points. Both the phase and amplitude errors for the azimuth domain are distributed according to $\mathcal{N}(0, 0.5)$ and $\mathcal{N}(0, 1)$ in Figs. 5(a) and 5(b). Further, we employ a total of $N_{\mathrm{y}} = 16$ antennas for the azimuth domain. As can be seen from Figs. 5(a) and 5(b), the azimuth radiation patterns are severely contaminated by the phase and amplitude errors such that the main lobe and side lobes can not be differentiated. In Figs. 5(c) and 5(d), we plot the ratio metrics versus the angle to be estimated assuming ideal radiation pattern and impaired radiation pattern with $N_{\mathrm{y}} = 16$ and $\delta_{\mathrm{y}} = \pi/8$. It is observed from Fig. 5(d) that with 0.5 phase and amplitude errors variances, the ratio metrics obtained via different impairment realizations are neither monotonic functions of the angle to be estimated nor symmetrical with respect to the origin. These observations are consistent with our analysis. Practical implementation of the proposed angle tracking designs therefore

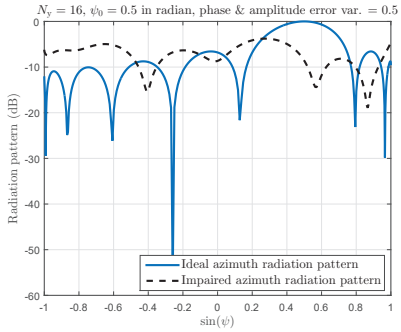

(a)

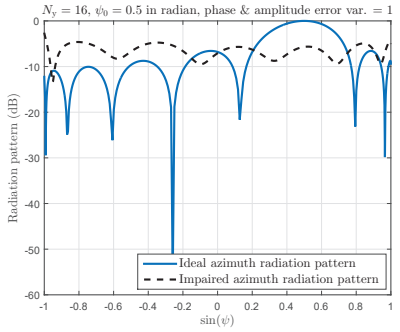

(b)

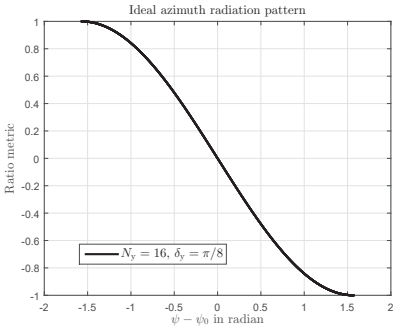

(c)

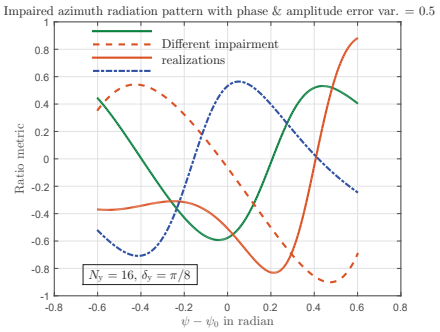

(d)

Fig. 5. (a) Ideal azimuth radiation pattern and impaired azimuth radiation pattern with $N_{\rm y} = 16$ and the phase & amplitude errors variances 0.5. (b) Ideal azimuth radiation pattern and impaired azimuth radiation pattern with $N_{\rm y} = 16$ and the phase & amplitude errors variances 1. (c) Ratio metric versus angles to be estimated under ideal azimuth radiation pattern with $N_{\rm y} = 16$ and $\delta_{\rm y} = \pi/8$. (d) Ratio metrics versus angles to be estimated under different realizations of impaired azimuth radiation patterns with $N_{\rm y} = 16$ and $\delta_{\rm y} = \pi/8$. The phase & amplitude errors variances are 0.5.

requires array calibration to compensate for the phase and amplitude errors.

Conventional array calibration methods such as those in [29] can not be directly applied to the array setup shown in Fig. 1. This is because in the employed array architecture, all antenna elements are driven by a limited number of RF chains such that only $N_{\rm RF}$-dimensional measurements are accessible to calibrate all $N_{\rm tot}$ antenna elements. In this paper, we develop and evaluate an off-line array calibration method for the employed array configurations assuming simple LOS channels and single-carrier setup.

In this method, we assume that a single calibration source transmitting the calibration reference signal (RS) is located at the origin with respect to the BS antenna array such that the calibration RS impinges on the antenna array at 0 degree in both the azimuth and elevation domains. At the BS, a set of receive combining vectors are formed in a TDM manner probing towards $N_{\rm tot}$ different angular directions in both the azimuth and elevation domains. The external calibration source can be placed close to the BS antenna array, and the channel between them is LOS. We can therefore express the signals received across all the $N_{\rm tot}$ receive probings as

$$\begin{aligned} y_0 =& \boldsymbol{a}_{\rm t}^*(\eta_{{\rm el},0},\eta_{{\rm az},0})\boldsymbol{C}\boldsymbol{a}_{\rm t}(\theta,\psi)x \\ &+ \boldsymbol{a}_{\rm t}^*(\eta_{{\rm el},0},\eta_{{\rm az},0})\boldsymbol{n}_0 \end{aligned} \tag{22}$$

$$\vdots$$

$$\begin{aligned} y_{N_{\rm tot}-1} =& \boldsymbol{a}_{\rm t}^*(\eta_{{\rm el},N_{\rm x}-1},\eta_{{\rm az},N_{\rm y}-1})\boldsymbol{C}\boldsymbol{a}_{\rm t}(\theta,\psi)x \\ &+ \boldsymbol{a}_{\rm t}^*(\eta_{{\rm el},N_{\rm x}-1},\eta_{{\rm az},N_{\rm y}-1})\boldsymbol{n}_{N_{\rm tot}-1}, \end{aligned} \tag{23}$$

where x represents the calibration RS, $\theta = \psi = 0$, $\eta_{{\rm el},i_{\rm el}}$ and $\eta_{{\rm az},i_{\rm az}}$ ($i_{\rm el} = 0,\cdots,N_{\rm x}-1$ and $i_{\rm az} = 0,\cdots,N_{\rm y}-1$) are the receive steering directions in the elevation and azimuth domains, and $\boldsymbol{n}_i$ ($i = 0,\cdots,N_{\rm tot}-1$) is the corresponding noise vector. In this paper, we assume the calibration RS $x = 1$ while it can be selected as a different symbol from 1 as long as it is known a prior. By concatenating all the received signal samples $y_0,\cdots,y_{N_{\rm tot}-1}$, we therefore have

$$\boldsymbol{y} = \begin{bmatrix} y_0 \\ \vdots \\ y_{N_{\rm tot}-1} \end{bmatrix} = \boldsymbol{A}_{\rm t}\boldsymbol{C}\boldsymbol{1}_{N_{\rm tot}\times 1} + \boldsymbol{A}_{\rm t}\boldsymbol{n}, \tag{24}$$

with

$$\begin{aligned} \boldsymbol{A}_{\rm t} &= \begin{bmatrix} \boldsymbol{a}_{\rm t}^*(\eta_{{\rm el},0},\eta_{{\rm az},0}) \\ \vdots \\ \boldsymbol{a}_{\rm t}^*(\eta_{{\rm el},N_{\rm x}-1},\eta_{{\rm az},N_{\rm y}-1}) \end{bmatrix} \in \mathbb{C}^{N_{\rm tot}\times N_{\rm tot}}, \\ \boldsymbol{n} &= \begin{bmatrix} \boldsymbol{n}_0 \\ \vdots \\ \boldsymbol{n}_{N_{\rm tot}-1} \end{bmatrix} \in \mathbb{C}^{N_{\rm tot}\times 1}. \end{aligned} \tag{25}$$

According to (24), the phase and amplitude errors matrix can be estimated as

$$\hat{\boldsymbol{C}} = {\rm diag}\left\{\boldsymbol{A}_{\rm t}^{-1}\boldsymbol{y}\right\}, \tag{26}$$

and the calibration matrix is determined as $\boldsymbol{K} = \hat{\boldsymbol{C}}^{-1}$. Note that with different receive steering directions and DFT-type

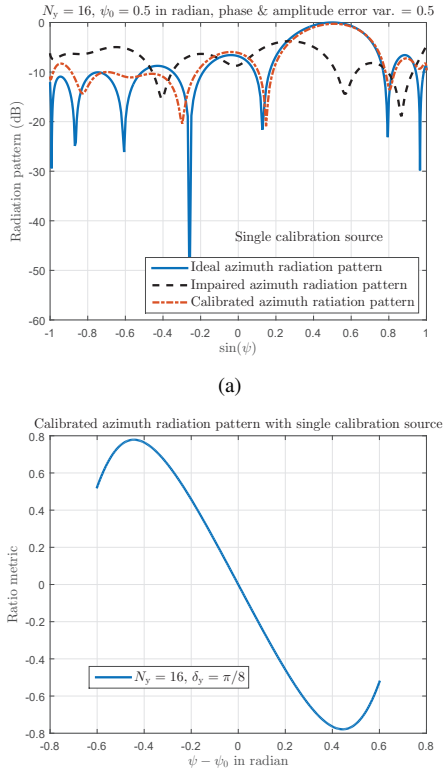

Fig. 6. (a) Calibrated azimuth radiation pattern using the proposed single calibration source and receive combining based calibration method; $N_{\mathrm{x}} = 1$, $N_{\mathrm{y}} = 16$ with the phase & amplitude errors variances 0.5. (b) Ratio metric versus angles to be estimated under calibrated azimuth radiation pattern with the proposed single calibration source based method; $N_{\mathrm{x}} = 1$, $N_{\mathrm{y}} = 16$ and $\delta_{\mathrm{y}} = \pi/8$; the phase & amplitude errors variances are 0.5.

receive steering vector structure, the square matrix $\boldsymbol{A}_{\mathrm{t}}$ is invertible.

In Fig. 6(a), we evaluate the impact of the residual calibration errors on the azimuth radiation pattern for the proposed calibration method. We set the calibration SNR as 0 dB. As can be seen from Fig. 6(a), the calibrated radiation pattern almost matches with the ideal radiation pattern in the azimuth domain such that the main lobe and side lobes can be clearly differentiated. Note that with increase in the calibration SNR, the calibration performances can be further improved.

After the array calibration, the amplitude and phase errors become small and are approximately the same across all the antenna elements. The corresponding ratio metric can therefore exhibit the same form as in the perfect radiation pattern case, implying that the channel directional information can be retrieved by inverting the ratio metric. In Fig. 6(b), we plot the ratio metrics obtained after the array calibration with respect to the angle to be estimated in the azimuth domain. By comparing Fig. 6(b) with Fig. 5(c), it can be observed that the monotonic and symmetric properties of the ratio metric hold for most of the angle values.

V. Numerical Results

In this section, we evaluate the proposed BS-driven angle tracking design with the direct ratio metric feedback and the periodic DTC. Note that different angle tracking strategies developed in Section III exhibit similar tracking performances, though they have different requirements on the tracking triggering metric, feedback information, and information available at the UE side. We evaluate the proposed angle tracking method assuming ideal radiation pattern, impaired radiation pattern with phase and amplitude errors, and calibrated radiation pattern. For simplicity, we obtain the calibrated radiation pattern via the proposed single calibration source based strategy. We set the angle difference threshold for triggering the beam adjustment as 10°. As the ratio metric is non-uniformly distributed within the interval of $[-1, 1]$ [16], we can employ the Lloyd's algorithm [30] to optimize the codebook for quantizing the ratio metric.

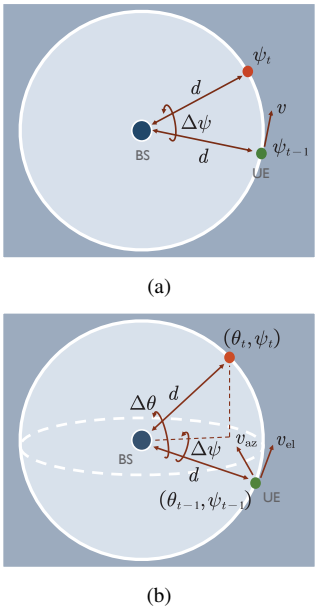

Fig. 7. (a) Angular motion model I. The BS is located at the origin of a ring, and the UE is moving along the ring with certain absolute speed v. The radius of the ring is denoted by d. (b) Angular motion model II. The BS is located at the origin of a sphere, and the UE is moving on the surface with certain absolute speeds v_{az} and v_{el} towards the azimuth and elevation domains. The radius of the sphere is denoted by d.

A. Narrowband single-path channels with single-carrier

In this part, we provide the numerical results in narrowband single-path channels with single-carrier modulation. We consider a single UE and two angular motion models shown in Figs. 7(a) and 7(b) to reveal the moving trajectory of the UE. In the first model (angular motion model I), the ULA is employed at the BS, while in the second model (angular motion model II), the UPA is employed at the BS such that the tracking beams can be probed towards both the elevation and azimuth domains. For both cases, the ULA is assumed at the UE side. Note that we develop the angular motion models I and II to better characterize the angle variations in terms of the moving trajectory. In Section V-C, we employ statistical temporal evolution tools to model practical channel variations. We list other simulation assumptions and parameters in Table II. We drop the path index here due to the single-path assumption.

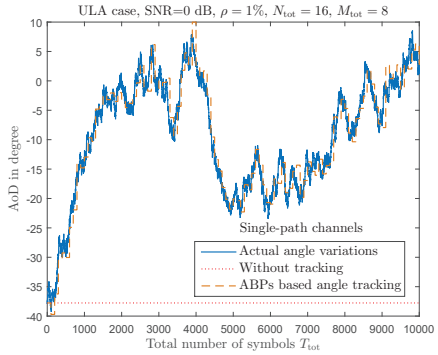

(a)

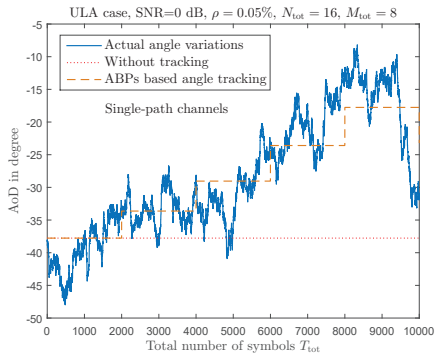

(b)

Fig. 8. Examples of actual angle variations, angle tracking using the proposed method, and without angle tracking in single-path channels; $N_{\rm tot} = 16$, $M_{\rm tot} = 8$ and 0 dB SNR are assumed with the ULA equipped at the BS and ideal radiation pattern. (a) $\rho = 1\%$ tracking overhead. (b) $\rho = 0.05\%$ tracking overhead.

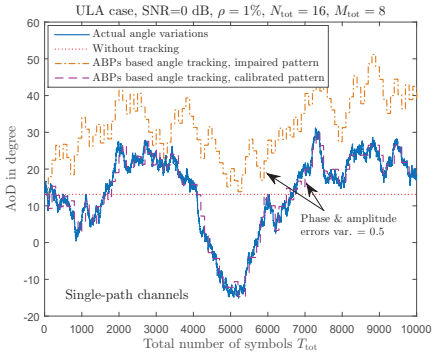

(a)

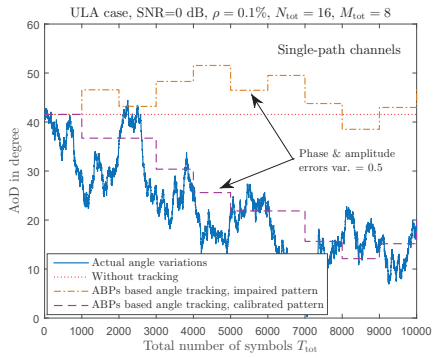

(b)

Fig. 9. $N_{\rm tot} = 16$, $M_{\rm tot} = 8$ and 0 dB SNR are assumed with the ULA equipped at the BS; ideal radiation pattern, impaired radiation pattern, and calibrated radiation pattern are evaluated. The phase & amplitude errors variances are set as 0.5. (a) Examples of actual angle variations, angle tracking using the proposed method, and without angle tracking; $\rho = 1\%$ tracking overhead. (b) Examples of actual angle variations, angle tracking using the proposed method, and without angle tracking; $\rho = 0.1\%$ tracking overhead.

Note that the angle variations $\Delta\psi$ and $\Delta\theta$ are obtained according to the UE's azimuth and elevation velocities $v_{\rm az}$ and $v_{\rm el}$, the BS-UE distance d, and the symbol duration. We further randomize the angle variations by incorporating a Gaussian distributed random variable w with zero mean and variance 1 as in Table II. In the simulations, we set $T = 1$. That is, each DTC comprises one time-slot (symbol), during which one auxiliary beam pair is formed. The two beams in the corresponding auxiliary beam pair are simultaneously probed, which are differentiated by the UE via the beam-specific pilot signal design. We can then define the tracking overhead as $\rho = 1/T_{\rm d}$. For instance, $T_{\rm d} = 1000$ results in less tracking overhead than $T_{\rm d} = 10$ as the corresponding tracking overheads are computed as $\rho = 0.1\%$ and $\rho = 10\%$. We assume angular motion model I for Figs. 8 and 9, and angular motion model II for Fig. 10.

In Fig. 8, we provide snapshots of the angle tracking results over time for $\rho = 1\%$ and 0.05% in the proposed design. For comparison, we also provide the actual angle variations and the case without angle tracking. Further, we assume ideal radiation pattern. As can be seen from Fig 8(a), the proposed auxiliary beam pair-assisted angle tracking design can accurately track the angle variations under relatively high tracking overhead, i.e., 1%. By reducing the tracking overhead to 0.05%, the tracking resolution becomes small, which in turn, degrades the angle tracking performances as shown in Fig 8(b). Under different tracking overhead assumptions, the trend of the angle variations can be well captured by the proposed angle tracking design.

In Figs. 9(a) and 9(b), we evaluate the proposed angle tracking design assuming both impaired and calibrated radiation patterns with 1% and 0.1% tracking overheads. We set the variances of the phase and amplitude errors as 0.5. Due to the random phase and amplitude errors, the angle tracking performance of the proposed approach with the impaired radiation pattern is deteriorated. Even with relatively high tracking overhead (e.g., 1% in Fig. 9(a)), the tracked angles are very different from the actual ones for all the channel realizations. By compensating for the phase and amplitude errors via the proposed calibration method, the angle tracking performance is significantly improved. For 1% tracking overhead, the angle tracking performance of the proposed method with calibrated radiation pattern almost matches with the actual angle variations for all the channel realizations.

We now evaluate the two-dimensional angle tracking performance for the proposed approach using calibrated radiation pattern. A total of $N_{\rm tot} = 32$ antenna elements are equipped at the BS side with the UPA placed in the xy-plane. Further, we set $N_{\rm x} = 4$ and $N_{\rm y} = 8$. In Fig. 10(a), we plot the cumulative density functions (CDFs) of the beamforming gains

TABLE II
SIMULATION ASSUMPTIONS AND PARAMETERS.

SYSTEM PARAMETERS	SIMULATION ASSUMPTIONS
BS-UE distance d (m)	100
UE's azimuth velocity v/v_{az} (km/h)	100
UE's elevation velocity v_{el} (km/h)	30
Symbol duration (μs)	3.7
Total number of symbols T_{tot}	10^4
Periodicity of the DTC T_{d} (number of symbols)	10, 100, 1000, 2000
Azimuth angle variation model	$\psi_t = \psi_{t-1} + \Delta\psi + w$
Elevation angle variation model	$\theta_t = \theta_{t-1} + \Delta\theta + w$
Pathloss model	[31]

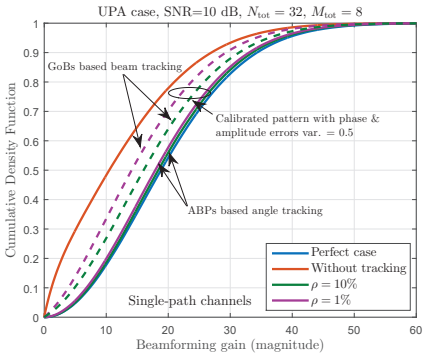

(a)

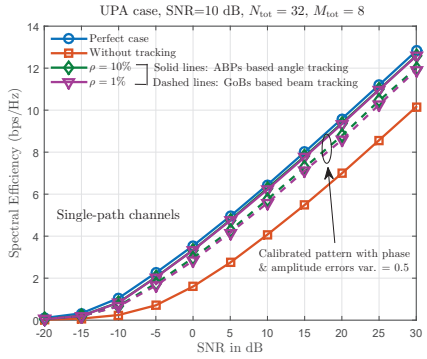

(b)

Fig. 10. Angular motion model II. (a) CDFs of the beamforming gains obtained via the anchor beams in the DDC with $N_{\text{tot}} = 32$, $M_{\text{tot}} = 8$ and 10 dB SNR. The proposed approach and the grid-of-beams (GoBs) based beam tracking are evaluated assuming calibrated antenna array. (b) Spectral efficiency performance obtained via the anchor beams in the DDC with $N_{\text{tot}} = 32$, $M_{\text{tot}} = 8$ and 10 dB SNR. The proposed approach and the grid-of-beams based beam tracking are evaluated assuming calibrated antenna array.

obtained from the anchor beam in the DDC. With calibrated radiation pattern, the proposed method shows close performance relative to the perfect case assuming various tracking overheads. In Fig. 10(b), the spectral efficiency performance is evaluated using the anchor beam in the DDC. Specifically, denoting by $h_{\text{eff}} = g\boldsymbol{a}_{\text{r}}^*(\nu)\boldsymbol{a}_{\text{r}}(\nu)\boldsymbol{a}_{\text{t}}^*(\theta,\psi)\boldsymbol{a}_{\text{t}}(\hat{\theta},\hat{\psi})$ for single-path channels, we can compute the spectral efficiency metric as $C = \mathbb{E}\left[\log_2\left(1+\gamma h_{\text{eff}}^* h_{\text{eff}}\right)\right]$. Similar to Fig. 10(a), the spectral efficiency performances obtained by using the proposed method with different tracking overheads are close to the perfect case. In Figs. 10(a) and 10(b), we also evaluate the grid-of-beams based beam tracking design assuming various tracking overheads. For fair comparison, we employ the same number of tracking beams as in the auxiliary beam pair based angle tracking design. As can be seen from Figs. 10(a) and 10(b), the proposed algorithm shows superior beamforming gain and spectral efficiency performances over the grid-of-beams based beam tracking strategy.

B. Narrowband multi-path channels with single-carrier

In this part, we employ a Rician multi-path channel model with various Rician K-factor values, which is given as

$$\boldsymbol{H} = \sqrt{\frac{\mathsf{K}}{1+\mathsf{K}}} \underbrace{g_r \boldsymbol{a}_{\text{r}}(\varphi_r)\boldsymbol{a}_{\text{t}}^*(\mu_r,\phi_r)}_{\boldsymbol{H}_{\text{LOS}}} + \sqrt{\frac{1}{1+\mathsf{K}}} \underbrace{\sum_{r'=1,r'\neq r}^{N_{\text{r}}} g_{r'}\boldsymbol{a}_{\text{r}}(\varphi_{r'})\boldsymbol{a}_{\text{t}}^*(\mu_{r'},\phi_{r'})}_{\boldsymbol{H}_{\text{NLOS}}}, \quad (27)$$

where $\boldsymbol{H}_{\text{LOS}}$ and $\boldsymbol{H}_{\text{NLOS}}$ represent LOS and NLOS channel components and K is the Rician factor. The number of NLOS channel components is set to 5. Further, we evaluate the mean angle tracking error (MATE), which is calculated as $\mathbb{E}[|\xi_t - \hat{\xi}_t|]$, where ξ_t is the channel's azimuth/elevation angle at time t, and $\hat{\xi}_t$ is its tracked counterpart. We use the angular motion model I to characterize the angle variations of all paths, and the objective is to track the variations of the dominant path.

It is observed from Fig. 11(a) that with increase in the number of channel paths, the MATE performance degrades because of the multi-path interference. Similar observation is obtained by reducing the Rician K-factor value from 13 dB to 6 dB. The performance differences between $N_{\text{r}} = 2$ and $N_{\text{r}} = 10$, and $\mathsf{K} = 6$ dB and $\mathsf{K} = 13$ dB, however, are marginal due to the fact that relatively narrow tracking beams are formed surrounding only the dominant path. Further, by increasing the total number of transmit antennas N_{tot} from 8 to 16, the MATE significantly decreases. At relatively high SNR, the multi-path interference would dominate the MATE performance. These observations are consistent with our approximation and analysis in Section III-A. In Fig. 11(b), we examine the impact of multiple auxiliary beam pairs probings on the MATE performance in a 6-path channel with 6 dB Rician K-factor. If the angle tracking is triggered, the MATE decreases with increase in the number of probings of identical auxiliary beam pairs, leveraging the spreading gain discussed in Section III-B to improve the angle tracking performance especially in low to medium SNR regimes.

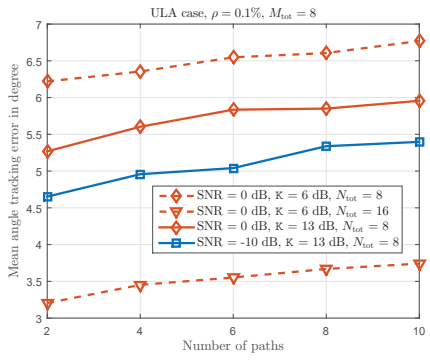

(a)

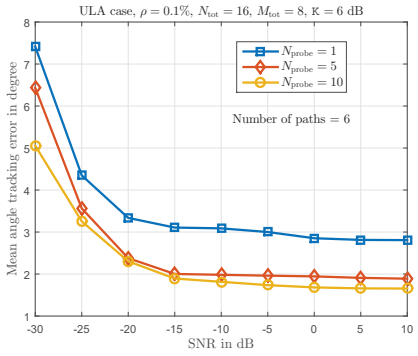

(b)

Fig. 11. ULAs are equipped at both the BS and UE with $M_{\rm tot} = 8$. Angular motion model I is used with calibrated radiation patterns (phase and amplitude error variances are 0.5). The tracking overhead is $\rho = 0.1\%$. (a) Mean angle tracking error (MATE) performance in narrowband Rician multi-path channels with various numbers of paths, Rician K-factor values, and etc. (b) MATE performance in narrowband Rician multi-path channels with $N_{\rm probe}$ as the number of probings of identical auxiliary beam pairs to track a given angle's variations if the angle tracking is triggered.

C. Wideband multi-path channels with OFDM

The temporal evolution effect of mmWave channels is not well characterized in current wideband mmWave channel models [32]. In this part ofãĂĂsimulation, we therefore first implement the temporally correlated mmWave channels by considering both (i) the NYUSIM open source platform developed in [31], [33] and (ii) the statistical temporal evolution model used in [14], [34].

For the NYUSIM open source platform, we consider the urban micro-cellular (UMi) scenario with NLOS components for the 28 GHz carrier frequency. We evaluate 125 MHz RF bandwidths with $N = 512$ subcarriers. The corresponding CP lengths is $D = 64$. The employed ZC-type sequences occupy the central 63 subcarriers with the root indices $i_0 = 25$ and $i_1 = 34$. We set the subcarrier spacing and symbol duration as 270 KHz and 3.7 μs following the numerology provided in [1]. Detailed channel modeling parameters are given in [31, Table III]. Further, our design focus here is to track the strongest path's AoD by using the proposed approach.

Before proceeding with the temporal channel evolution model, we first rewrite the time-domain channel matrix in (2) in a more compact form. For time-slot t, denoting by $\boldsymbol{\varphi}_t = [\varphi_{1,t}, \varphi_{2,t}, \cdots, \varphi_{N_{\rm r},t}]^{\rm T}$, $\boldsymbol{\mu}_t = [\mu_{1,t}, \mu_{2,t}, \cdots, \mu_{N_{\rm r},t}]^{\rm T}$ and $\boldsymbol{\phi}_t = [\phi_{1,t}, \phi_{2,t}, \cdots, \phi_{N_{\rm r},t}]^{\rm T}$, we have $\boldsymbol{H}_t[d] = \boldsymbol{A}_{\rm R}(\boldsymbol{\varphi}_t)\boldsymbol{G}_t[d]\boldsymbol{A}_{\rm T}^*(\boldsymbol{\mu}_t, \boldsymbol{\phi}_t)$, where $\boldsymbol{A}_{\rm R}(\boldsymbol{\varphi}_t)$ and $\boldsymbol{A}_{\rm T}(\boldsymbol{\mu}_t, \boldsymbol{\phi}_t)$ represent the array response matrices for the receiver and transmitter such that

$$\boldsymbol{A}_{\rm R}(\boldsymbol{\varphi}_t) = [\boldsymbol{a}_{\rm r}(\varphi_{1,t}) \quad \boldsymbol{a}_{\rm r}(\varphi_{2,t}) \quad \cdots \quad \boldsymbol{a}_{\rm r}(\varphi_{N_{\rm r},t})] \tag{28}$$

$$\boldsymbol{A}_{\rm T}(\boldsymbol{\mu}_t, \boldsymbol{\phi}_t) = \Big[\boldsymbol{a}_{\rm t}(\mu_{1,t}, \phi_{1,t}) \quad \boldsymbol{a}_{\rm t}(\mu_{2,t}, \phi_{2,t}) \quad \cdots \quad \boldsymbol{a}_{\rm t}(\mu_{N_{\rm r},t}, \phi_{N_{\rm r},t})\Big], \tag{29}$$

and $\boldsymbol{G}_t[d] = \text{diag}\left(\left[g_1 p\left(dT_{\rm s} - \tau_1\right), \cdots, g_{N_{\rm r}} p\left(dT_{\rm s} - \tau_{N_{\rm r}}\right)\right]^{\rm T}\right)$. We model the temporal evolution of the path gains as the first-order Gauss-Markov process as [14]

$$\boldsymbol{G}_{t+1}[d] = \rho_{\rm D}\boldsymbol{G}_t[d] + \sqrt{1 - \rho_{\rm D}^2}\boldsymbol{B}_{t+1}, \tag{30}$$

where $\rho_{\rm D} = J_0\left(2\pi f_{\rm D} T_{\rm s}\right)$ and $\boldsymbol{B}_{t+1}$ is a diagonal matrix with the diagonal entries distributed according to $\mathcal{N}_c(0, 1)$. Here, $J_0(\cdot)$ denotes the zeroth-order Bessel function of first kind and $f_{\rm D}$ is the maximum Doppler frequency. The elevation and azimuth AoDs vary according to [34]

$$\boldsymbol{\mu}_{t+1} = \boldsymbol{\mu}_t + \Delta\boldsymbol{\mu}_{t+1}, \quad \boldsymbol{\phi}_{t+1} = \boldsymbol{\phi}_t + \Delta\boldsymbol{\phi}_{t+1}, \tag{31}$$

where $\Delta\boldsymbol{\mu}_{t+1}$ and $\Delta\boldsymbol{\phi}_{t+1}$ are distributed according to $\mathcal{N}_c(\boldsymbol{0}_{N_{\rm r}}, \sigma_\mu^2\boldsymbol{I}_{N_{\rm r}})$ and $\mathcal{N}_c(\boldsymbol{0}_{N_{\rm r}}, \sigma_\phi^2\boldsymbol{I}_{N_{\rm r}})$. We first determine the initial path gains, path delays, azimuth/elevation AoDs, and AoAs through one simulation run using the NYUSIM open source platform. We then obtain the channels for the subsequent time-slots by using the initial channel results and the temporal evolution model presented in (30) and (31).

In Fig. 12, we plot the beamforming gains against the employed OFDM symbols for $\rho = 0.1\%$ tracking overhead. We set $f_{\rm D} = 1.3$ KHz and $\sigma_\mu^2 = \sigma_\phi^2 = (\pi/180)^2$, which characterize relatively fast moving and angle variation speeds [14], [34]. In addition to the actual angle variations, we evaluate the proposed angle tracking and grid-of-beams based beam tracking designs with calibrated radiation patterns. Similar to the evaluation results shown in Section V-A, the proposed algorithm shows close tracking performance to the perfect case, and outperforms the existing beam tracking approach for various system setups.

In Fig. 13, we examine the impact of the employed ZC sequence length on the angle tracking performance in wideband channels. The simulation parameters are configured similar to those in Fig. 12. As can be seen from Fig. 13(a), the MATE decreases with increase in the employed ZC sequence length for angle tracking assuming various SNRs. These observations are consistent with our analysis in Section III-A such that the inter-beam interference can be significantly reduced if the simultaneously probed two beams use relatively long tracking sequences. Similar conclusions are obtained from Fig. 13(b) that for a wide range of SNR values, the proposed angle tracking strategy with large sequence length exhibits a better MATE performance.

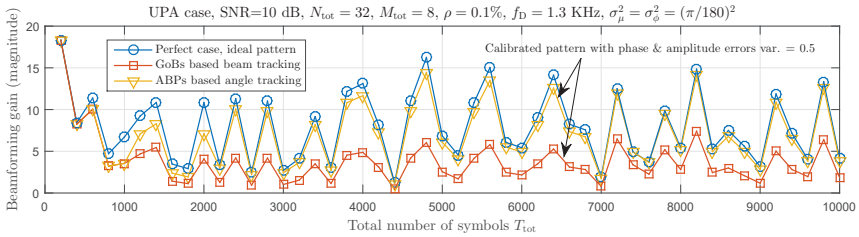

Fig. 12. Beamforming gains obtained via the anchor beams in the DDC with $N_{\rm tot}=32$, $M_{\rm tot}=8$ and 10 dB SNR. The proposed approach and the grid-of-beams based beam tracking are evaluated assuming calibrated radiation pattern. $f_{\rm D}=1.3$ KHz and $\sigma_\mu^2=\sigma_\phi^2=(\pi/180)^2$. $\rho=1\%$ tracking overhead.

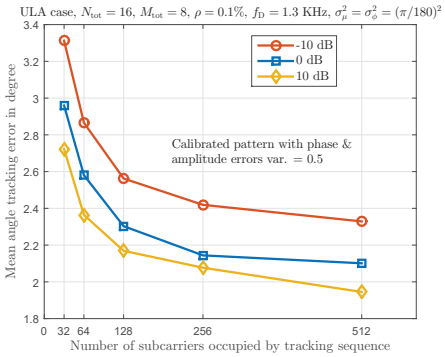

(a)

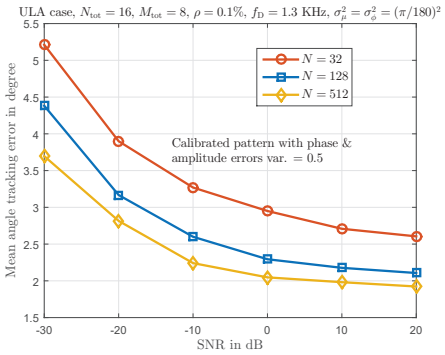

(b)

Fig. 13. ULAs are deployed by both the BS and UE with $N_{\rm tot}=16$ and $M_{\rm tot}=8$. $f_{\rm D}=1.3$ KHz and $\sigma_\mu^2=\sigma_\phi^2=(\pi/180)^2$ are assumed. The tracking overhead is $\rho=0.1\%$ with calibrated antenna array. (a) MATE performance against different lengths of the employed ZC sequences for tracking. (b) MATE performance versus various SNRs for the proposed angle tracking design.

VI. Conclusions

In this paper, we developed and evaluated several new angle tracking design approaches for mobile wideband mmWave systems with antenna array calibration. The proposed methods are different in terms of tracking triggering metric, feedback information, and auxiliary beam pair setup required at the UE. These differences allow the proposed strategies to be adopted in different deployment scenarios. We exposed the detailed design procedures of the proposed methods and showed that they can obtain high-resolution angle tracking results. The proposed methods neither depend on a particular angle variation model nor require the on-grid assumption. Since the proposed methods are sensitive to radiation pattern impairments, we showed by numerical examples that with appropriate array calibration, the angle variations can still be successfully tracked via the proposed methods under various angle variation models.

References

[1] Z. Pi and F. Khan, "An introduction to millimeter-wave mobile broadband systems," *IEEE Commun. Mag.*, vol. 49, no. 6, pp. 101–107, Jun. 2011.

[2] R. W. Heath Jr., N. Gonzalez-Prelcic, S. Rangan, W. Roh, and A. Sayeed, "An overview of signal processing techniques for millimeter wave MIMO systems," *IEEE J. Sel. Top. Signal Process.*, vol. 10, no. 3, pp. 436–453, Feb. 2016.

[3] Z. Pi, J. Choi, and R. W. Heath Jr., "Millimeter-wave Gbps broadband evolution towards 5G: fixed access and backhaul," *IEEE Commun. Mag.*, vol. 54, no. 4, pp. 138–144, Apr. 2016.

[4] F. Boccardi, R. W. Heath Jr., A. Lozano, T. L. Marzetta, and P. Popovski, "Five disruptive technology directions for 5G," *IEEE Commun. Mag.*, vol. 52, no. 2, pp. 74–80, Feb. 2014.

[5] T. S. Rappaport, R. W. Heath Jr., R. C. Daniels, and J. N. Murdock, *Millimeter wave wireless communications*, Prentice Hall, 2014.

[6] "Wireless LAN Medium Access Control (MAC) and Physical Layer (PHY) Specifications - Amendment 4: Enhancements for Very High Throughput in the 60 GHz Band," IEEE P802.11ad/D9.0.

[7] J. Wang, Z. Lan, C. Pyo, T. Baykas, C. Sum, M. Rahman, J. Gao, R. Funada, F. Kojima, H. Harada, and S. Kato, "Beam codebook based beamforming protocol for multi-Gbps millimeter-wave WPAN systems," *IEEE J. Sel. Areas Commun.*, vol. 27, no. 8, pp. 1390–1399, Oct. 2009.

[8] "Overview of NR initial access," 3GPP TSG RAN WG1 meeting #87, R1-1611272, Nov. 2016.

[9] J. Palacios, D. D. Donno, and J. Widmer, "Tracking mm-Wave channel dynamics: fast beam training strategies under mobility," in *Proc. of IEEE Conf. on Computer Commun. (INFOCOM 2017)*, Oct. 2017.

[10] J. Bae, S.-H. Lim, J.-H. Yoo, and J.-W. Choi, "New beam tracking technique for millimeter wave-band communications," *arXiv preprint arXiv:1702.00276*, Feb. 2017.

[11] L. Dai and X. Gao, "Priori-aided channel tracking for millimeter-wave beamspace massive MIMO systems," in *Proc. of IEEE URSI Asia-Pacific Radio Science Conference (URSI AP-RASC)*, Aug. 2016.

[12] X. Gao, L. Dai, T. Xie, X. Dai, and Z. Wang, "Fast channel tracking for Terahertz beamspace massive MIMO systems," *IEEE Trans. Veh. Technol.*, vol. 66, no. 7, pp. 5689–5696, Oct. 2016.

[13] Y. Zhou, P. C. Yip, and H. Leung, "Tracking the direction-of-arrival of multiple moving tragets by passive arrays: asymptotic performance analysis," *IEEE Trans. Signal Process.*, vol. 47, no. 10, pp. 2644–2654, Oct. 1999.

[14] C. Zhang, D. Guo, and P. Fan, "Mobile millimeter wave channel acquisition, tracking, and abrupt change detection," *arXiv preprint arXiv:1610.09626*, Oct. 2016.

[15] V. Va, H. Vikalo, and R. W. Heath Jr., "Beam tracking for mobile millimeter wave communication systems," in *Proc. of IEEE Global Conf. on Signal and Information Process.*, Dec. 2016.

[16] D. Zhu, J. Choi, and R. W. Heath Jr., "Auxiliary beam pair enabled AoD and AoA estimation in closed-loop large-scale mmWave MIMO system," *IEEE Trans. Wireless Commun.*, vol. 16, no. 7, pp. 4770–4785, Jul. 2017.

[17] D. Zhu, J. Choi, and R. W. Heath Jr., "Two-dimensional AoD and AoA acquisition for wideband millimeter-wave systems with dual-polarized MIMO," *IEEE Trans. Wireless Commun.*, vol. 16, no. 12, pp. 7890–7905, Dec. 2017.

[18] V. Rabinovich and N. Alexandrov, *Antenna arrays and automotive applications*, Springer New York, 2013.

[19] J. Singh and S. Ramakrishna, "On the feasibility of codebook-based beamforming in millimeter wave systems with multiple antenna arrays," *IEEE Trans. Wireless Commun.*, vol. 14, no. 5, pp. 2670–2683, May 2015.

[20] "Technical Report Group RAN: Spatial Channel Model For Multiple Input Multiple Output (MIMO) Simulations, v13.0.0," 3GPP, Jan. 2016. [Online]. Available: http://www.3gpp.org/DynaReport/25996.htm.

[21] B. M. Popovic, "Generalized chirp-like polyphase sequences with optimum correlation properties," *IEEE Trans. Inf. Theory*, vol. 38, no. 4, pp. 1406–1409, Jul. 1992.

[22] "Study on channel model for frequency spectrum above 6 GHz," 3GPP TR 38.900 V14.2.0, Dec. 2016.

[23] A. Sayeed, J. Brady, P. Cheng, and U. Tayyab, "Indoor channel measurements using a 28 GHz multi-beam MIMO prototype," in *IEEE Veh. Tech. Conf.*, Sep. 2016, pp. 1–5.

[24] A. Sayeed and J. Brady, "Beamspace MIMO channel modeling and measurement: methodology and results at 28 GHz," in *IEEE Global Telecomm. Conf.*, Dec. 2016.

[25] "Technical Specification Group RAN: Evolved Universal Terrestrial Radio Access (E-UTRA); Physical Channels and Modulation," 3GPP, Dec. 2011. [Online]. Available: http://www.3gpp.org/ftp/Specs/html-info/36211.htm.

[26] M. Hyder and K. Mahata, "Zadoff-Chu sequence design for random access initial uplink synchronization in LTE-like systems," *IEEE Trans. Wireless Commun.*, vol. 16, no. 1, pp. 503–511, Jan. 2017.

[27] G. Sommerkorn, D. Hampicke, R. Klukas, A. Richter, A. Schneider, and R. Thoma, "Reduction of DoA estimation errors caused by antenna array imperfections," in *Proc. of IEEE European Microwave Conf.*, Oct. 1999, pp. 287–290.

[28] B. Ng and C. See, "Sensor-array calibration using a maximum-likelihood approach," *IEEE Trans. Antennas Propag.*, vol. 44, no. 6, pp. 827–835, Jun. 1996.

[29] K. Sakaguchi, K. Kuroda, J.-I. Takada, and K. Araki, "Comprehensive calibration for MIMO system," in *Proc. of IEEE WPMC 2002*, Oct. 2002.

[30] S. Lloyd, "Least squares quantization in PCM," *IEEE Trans. Info. Theory*, vol. 28, no. 2, pp. 129–137, Mar. 1982.

[31] M. K. Samimi and T. S. Rappaport, "3-D millimeter-wave statistical channel model for 5G wireless system design," *IEEE Transactions on Microwave Theory and Techniques*, vol. 64, no. 7, pp. 2207–2225, Jul. 2016.

[32] T. S. Rappaport, S. Sun, and M. Shafi, "Investigation and comparison of 3GPP and NYUSIM channel models for 5G wireless communications," *arXiv preprint arXiv:1707.00291*, Jul. 2017.

[33] "NYUSIM channel simulator," http://wireless.engineering.nyu.edu./5g-millimeter-wave-channel-modeling-software/.

[34] J. He, T. Kim, H. Ghauch, K. Liu, and G. Wang, "Millimeter wave MIMO channel tracking systems," in *Proc. of IEEE Global Telecomm. Conf.*, Dec. 2014, pp. 1–5.

Dalin Zhu received the B.Eng. in Information Engineering from Beijing University of Posts and Telecommunications (BUPT) and M.Sc. in Electrical and Computer Engineering from Kansas State University in 2007 and 2009, respectively. He is currently pursuing the Ph.D. degree with the Wireless Networking and Communication Group, Department of Electrical and Computer Engineering, The University of Texas at Austin.

From 2010 to 2014, he worked as a research staff member and project manager in the Dept. of Wireless Communications at NEC Laboratories China (NLC) focusing on 3GPP LTE/LTE-A standardization, TD-LTE system-level simulator development and C-RAN prototyping. From 2012 to 2013, he was a visiting scientist at the Wireless Systems Laboratory (WSL), Stanford University. From 2014 to 2015, he worked at Samsung R&D Institute China - Beijing (SRC-B) as a staff engineer working towards 5G related topics including new waveform design, massive MIMO, non-orthogonal multiple access schemes, and mmWave communications. During the summers of 2018, 2017 and 2016, he worked as an intern at AT&T Labs, Austin, TX and Huawei Technologies, Rolling Meadows, IL focusing on 5G new radio simulation and research.

Mr. Zhu was the recipient of the University Graduate Continuing Fellowship (2018-2019), Cullen M. Crain Endowed Scholarship in Engineering (2017-2018) from the University of Texas at Austin, Award of Excellence (2015/Q1) from Samsung R&D Institute China - Beijing, best paper award from Chinacom 2013 (Green Communications Symposium), and Dean's Special Award of Merit (2010-2011) from NEC Laboratories China.

Junil Choi (S'11 - M'16) received the B.S. (with honors) and M.S. degrees in electrical engineering from Seoul National University in 2005 and 2007, respectively, and received the Ph.D. degree in electrical and computer engineering from Purdue University in 2015. He is now with the department of electrical engineering at POSTECH as an assistant professor.

From 2007 to 2011, he was a member of technical staff at Samsung Advanced Institute of Technology (SAIT) and Samsung Electronics Co. Ltd. in Korea, where he contributed to advanced codebook and feedback framework designs for the 3GPP LTE/LTE-Advanced and IEEE 802.16m standards. Before joining POSTECH, he was a postdoctoral fellow at The University of Texas at Austin. His research interests are in the design and analysis of massive MIMO, mmWave communication systems, distributed reception, and vehicular communication systems.

Dr. Choi was a co-recipient of a 2015 IEEE Signal Processing Society Best Paper Award, the 2013 Global Communications Conference (GLOBECOM) Signal Processing for Communications Symposium Best Paper Award, the 2018 JCCI Best Paper Award, and a 2008 Global Samsung Technical Conference best paper award. He was awarded the Michael and Katherine Birck Fellowship from Purdue University in 2011; the Korean Government Scholarship Program for Study Overseas in 2011-2013; the Purdue College of Engineering Outstanding Student Research Award in 2014; and the IEEE ComSoc AP region Outstanding Young Researcher Award in 2017.

Qian Cheng is a Researcher and Standard Delegate at Huawei Technologies and has been focusing on 3GPP NR and LTE standardization for the past 7 years. Before working for Huawei Technologies, he worked as a research engineer for Qualcomm corporate R&D, focusing on LTE chipset algorithm design for both eNb and UE. He also spent several years with 3Com/US Robotics corporation working on the wire-line analog modem algorithm development and implementation with DSP chipset.

Weimin Xiao received the Ph.D. degree in electrical engineer from Northwestern University, Evanston, IL. Before joining Huawei, he worked for Motorola developing technologies and standards of EVDV, HSPA, and LTE. He currently holds the position of principle engineer and director of Huawei US radio access research and standards focusing on technologies for cooperative massive MIMO, advanced carrier design and resource optimization, high frequency communications, and connected cars, and their standardization in 5G and beyond. He received the IEEE Communication Society & Information Theory Society Joint Paper Award in 2002. He has more than 80 patents in the areas of power control, MIMO and CSI feedback, cooperative communications, interference control, radio resource optimization, and etc.

Robert W. Heath Jr. (S'96 - M'01 - SM'06 - F'11) received the B.S. and M.S. degrees from the University of Virginia, Charlottesville, VA, in 1996 and 1997 respectively, and the Ph.D. from Stanford University, Stanford, CA, in 2002, all in electrical engineering. From 1998 to 2001, he was a Senior Member of the Technical Staff then a Senior Consultant at Iospan Wireless Inc, San Jose, CA where he worked on the design and implementation of the physical and link layers of the first commercial MIMO-OFDM communication system. Since January 2002, he has been with the Department of Electrical and Computer Engineering at The University of Texas at Austin where he is a Cullen Trust for Higher Education Endowed Professor, and is a Member of the Wireless Networking and Communications Group. He is also President and CEO of MIMO Wireless Inc. He authored "Introduction to Wireless Digital Communication" (Prentice Hall, 2017) and "Digital Wireless Communication: Physical Layer Exploration Lab Using the NI USRP" (National Technology and Science Press, 2012), and co-authored "Millimeter Wave Wireless Communications" (Prentice Hall, 2014).

Dr. Heath has been a co-author of sixteen award winning conference and journal papers including the 2010 and 2013 EURASIP Journal on Wireless Communications and Networking best paper awards, the 2012 Signal Processing Magazine best paper award, a 2013 Signal Processing Society best paper award, 2014 EURASIP Journal on Advances in Signal Processing best paper award, the 2014 Journal of Communications and Networks best paper award, the 2016 IEEE Communications Society Fred W. Ellersick Prize, the 2016 IEEE Communications and Information Theory Societies Joint Paper Award, and the 2017 Marconi Prize Paper Award. He received the 2017 EURASIP Technical Achievement award. He was a distinguished lecturer in the IEEE Signal Processing Society and is an ISI Highly Cited Researcher. In 2017, he was selected as a Fellow of the National Academy of Inventors. He is also an elected member of the Board of Governors for the IEEE Signal Processing Society, a licensed Amateur Radio Operator, a Private Pilot, a registered Professional Engineer in Texas.